ANKARA YILDIRIM BEYAZIT UNIVERSITY

GRADUATE SCHOOL OF NATURAL AND APPLIED SCIENCES

SIMULATION OF AN INNOVATIVE FLOW-FIELD DESIGN BASED ON A BIO-INSPIRED PATTERN FOR PEM WATER ELECTROLYSIS

M.Sc. Thesis by

Mohammad Naser ALOBEID

Department of Mechanical Engineering

January, 2024

ANKARA

SIMULATION OF AN INNOVATIVE FLOW-FIELD DESIGN BASED ON A BIO-INSPIRED PATTERN FOR PEM WATER ELECTROLYSIS

A Thesis Submitted to

The Graduate School of Natural and Applied Sciences of

Ankara Yıldırım Beyazıt University

In Partial Fulfillment of the Requirements for the Degree of Master of Science in Mechanical Engineering, Department of Mechanical Engineering

by

Mohammad Naser ALOBEID

January, 2024

ANKARA

M.Sc. THESIS EXAMINATION RESULT FORM

We have read the thesis entitled "**SIMULATION OF AN INNOVATIVE FLOW-FIELD DESIGN BASED ON A BIO-INSPIRED PATTERN FOR PEM WATER ELECTROLYSIS**" completed by **MOHAMMAD NASER ALOBEID** under the supervision of **PROF. DR. SELAHATTIN ÇELIK** and we certify that in our opinion it is fully adequate, in scope and in quality, as a thesis for the degree of Master of Science.

Prof. Dr. Selahattin ÇELIK
———————————————————
Supervisor

Assoc. Prof. Dr. Hasan Özcan   Assoc. Prof. Dr Serhat Karyeyen
———————————————————   ———————————————————
Jury Member   Jury Member

Prof. Dr. Selahattin ÇELIK
———————————————————
Director

Graduate School of Natural and Applied Sciences

ETHICAL DECLARATION

I hereby declare that, in this thesis which has been prepared in accordance with the Thesis Writing Manual of Graduate School of Natural and Applied Sciences,

- All data, information and documents are obtained in the framework of academic and ethical rules,

- All information, documents and assessments are presented in accordance with scientific ethics and morals,

- All the materials that have been utilized are fully cited and referenced,

- No change has been made on the utilized materials,

- All the works presented are original,

and in any contrary case of above statements, I accept to renounce all my legal rights.

Date: 9 January 2024   **Signature………………………………………..**

Name & Surname: Mohammad Alobeid

ACKNOWLEDGMENTS

SIMULATION OF AN INNOVATIVE FLOW-FIELD DESIGN BASED ON A BIO-INSPIRED PATTERN FOR PEM WATER ELECTROLYSIS

ABSTRACT

Electrolysis paired with renewable energy sources emerges as a highly auspicious method for green hydrogen production. Within the spectrum of electrolysis approaches, the Polymer Electrolyte Membrane Water Electrolyzer (PEMWE) has garnered considerable attention due to its capacity for producing compressed, high-purity hydrogen. The design of bipolar plates and their channel patterns notably influence the performance and durability of the PEM water electrolyzer. Well-designed flow fields play a pivotal role in ensuring the uniform distribution of pressure and velocity within the stack, enabling high-pressure operation capabilities and facilitating high current densities. In this study, a precise leaf bio-inspired geometry is employed as a novel bipolar plate channel pattern, featuring a circular cross-section of 13.85 square centimeters. A comprehensive three-dimensional numerical model using COMSOL Multiphysics software was developed. Simulation outcomes demonstrate robust agreement when compared against previously simulated experimental data from published works. After a comparison of five different leaf bio-inspired models and traditional models, the result was obtained. The findings underscore that the exact leaf flow field model manifests the most uniform velocity profile, lower pressure drop, superior pressure distribution, and heightened mixture homogeneity in contrast to traditional models. According to the polarization curves obtained at the end of the numerical study, it was concluded that the exact leaf bio-inspired flow field design is positioned as a preferred option compared to other traditional designs.

Keywords: Flow field, PEMWE, Bio-inspired, CFD, Bipolar Plates, performance, pressure drop.

PEM SU ELEKTROLİZİ İÇİN BİYOLOJİDEN İLHAM ALAN BİR DESEN TABANLI YENİLİKÇİ AKIŞ ALANI TASARIMININ SİMÜLASYONU

ÖZ

Yenilenebilir enerji kaynaklarıyla eşleştirilen elektroliz, yeşil hidrojen üretimi için oldukça önemli bir yöntem olarak ortaya çıkıyor. Elektroliz yaklaşımları yelpazesinde, Polimer Elektrolit Membran Su Elektrolizörü (PEMWE), sıkıştırılmış, yüksek saflıkta hidrojen üretme kapasitesi nedeniyle büyük ilgi görmektedir. Bipolar plakaların tasarımı ve kanal desenleri, PEM su elektrolizörünün performansını ve dayanıklılığını önemli ölçüde etkilemektedir. İyi tasarlanmış akış alanları, hücre içinde basıncın ve hızın eşit dağılımını sağlamada, yüksek basınçlı çalışma yetenekleri sağlamada ve yüksek akım yoğunluklarını kolaylaştırmada çok önemli bir rol oynar. Bu çalışmada, 13,85 santimetrekarelik dairesel bir kesite sahip, yeni bir bipolar plaka kanal modeli olarak gerçek bir yaprak biyo-esinli geometri kullanılmıştır. COMSOL Multiphysics yazılımını kullanan kapsamlı bir üç boyutlu sayısal model geliştirilmiştir. Simülasyon sonuçları, yayınlanmış çalışmalardan önceden simüle edilmiş deneysel verilerle karşılaştırıldığında güçlü bir uyum göstermektedir. Beş farklı yaprak biyo-esinli model ile geleneksel modellerin karşılaştırılması sonrasında sonuçlar karşılaştırılmıştır. Bulgular, tam yaprak akış alanı modelinin, geleneksel modellerin aksine en düzgün hız profilini, daha düşük basınç düşüşünü, üstün basınç dağılımını ve yüksek karışım homojenliğini ortaya çıkarmıştır. Sayısal çalışma sonunda elde edilen polarizasyon eğrilerine göre gerçek yaprak biyo-ilhamlı akış alanı tasarımını diğer geleneksel tasarımlara göre tercih edilen bir seçenek olarak konumlandırdığı sonucuna ulaşılmıştır.

Anahtar Kelimeler: Akış alanı, Proton değişim membran su elektrolizörü, Biyo-esinli, HAD, çift kutuplu plakalar, performans, basınç düşüşü.

CONTENTS

LIST OF TABLES

LIST OF FIGURES

CHAPTER 1

INTRODUCTION

1.1 Motivation

The motivation for conducting an investigation into simulating a novel flow-field design based on a bio-inspired pattern for proton exchange membrane (PEM) water electrolysis stems from the increasing importance of environmentally friendly energy and the production of sustainable hydrogen. PEM water electrolysis has emerged as a promising technology for efficient hydrogen production in the quest for cleaner and more environmentally sustainable alternatives to traditional energy sources. The integration of a biomimetic pattern into the flow-field design aims to enhance the effectiveness and productivity of the electrolysis process by emulating optimized structures found in nature. By simulating and analyzing the proposed design, researchers aim to advance green hydrogen technology, accelerating the shift towards a more sustainable and environmentally friendly energy model. This study not only supports the worldwide transition to environmentally friendly energy sources but also has the potential to greatly impact the development of clean and renewable hydrogen, which is a crucial element in the quest for a more sustainable future.

1.2 Energy

The sustained escalation in global energy demand and consumption correlates significantly with expanding populations, enhanced living standards, and the industrial upsurge observed in developing nations. Forecasts project a potential amplification of global energy demand to one and a half times its present magnitude in the foreseeable future. Historically, a substantial portion of this demand has relied on fossil fuel utilization. However, this reliance has resulted in the release of significant volumes of greenhouse gas emissions, aggravating global warming and contributing to environmental degradation. Addressing these critical concerns and nurturing

sustainable development requires swift advancements in alternative green energy technologies. In tandem, numerous nations are prioritizing the implementation of environmentally conscientious energy policies to facilitate a sustainable environment and achieve decarbonization objectives. [1 - 2].

Hydrogen emerges as a promising and environmentally sustainable renewable energy carrier, recognized as the most abundant element in the universe. Comprising a solitary proton and electron, the hydrogen atom is the lightest element, possessing distinctive attributes such as a high energy density of 120 MJ/kg and a comparatively reduced volumetric energy density of 8 MJ/L . Despite its cosmic abundance, elemental hydrogen is not inherently available on Earth in its unadulterated form; instead, it exists in chemically bonded states within water, fossil fuel reservoirs, and biomass. [3 - 6]

Global hydrogen consumption had a significant increase in 2022 which illistrated in Figure 1.1. reaching 95 million metric tons, which is a 3% growth compared to the previous year. This growth trajectory materialized after the interruptions in 2020 caused by the Covid-19 epidemic and associated economic recession. Significantly, the use of hydrogen shown growth in all major areas, with the exception of Europe. In Europe, the chemical industry had less activity, and the cost of natural gas increased due to the war between Russia and Ukraine. As a result, hydrogen consumption decreased by around 6%. In contrast, North America and the Middle East had significant increases, but China remained the dominant player, accounting for more than 30% of the total world hydrogen use. Despite a slowdown in China's economic development, it remained the greatest consumer.
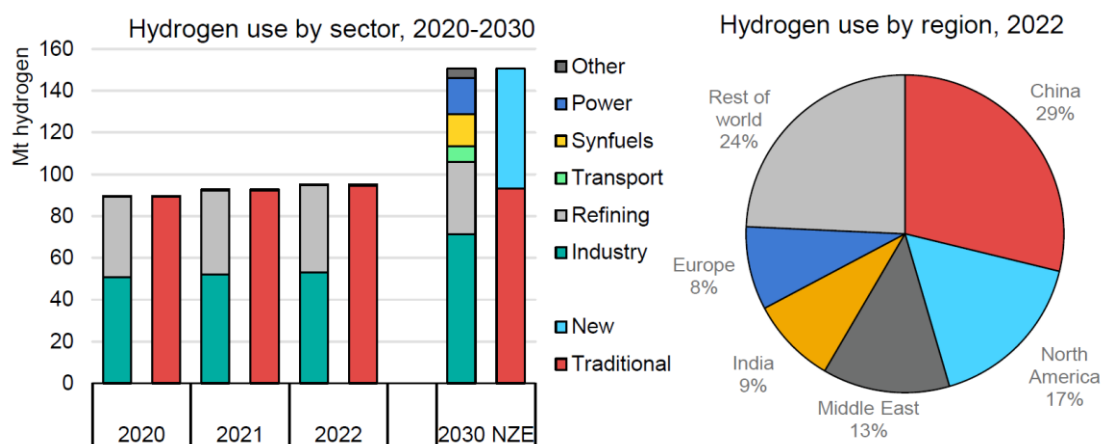
Figure 1.1 Sectorly and regionly usege of Hydrogen note that (NZE) Net Zero Emissions by 2050 Scenario. "Other" includes buildings and biofuels upgrading

In 2022, hydrogen deployment in refining operations climbed to nearly 41 million metric tons, exceeding the previous milestone established in 2018. Notably, the year-on-year rise was largely driven by considerable advances in North America and the Middle East, amounting to about 1 million metric tons, accounting for roughly three-quarters of the worldwide escalation. However, China witnessed a reduction in hydrogen demand by around 0.5 million metric tons owing to lower refinery throughput amidst severe pandemic-induced mobility limitations. Remarkably, approximately 80% of the hydrogen employed in refineries was created onsite, with 55% coming from dedicated hydrogen production, while the balance was generated as a by-product. In comparison, less than 1% of the hydrogen utilized in refining operations in 2022 was produced from low-emission technologies. The other 20% of hydrogen usage in refineries comes from merchant hydrogen, mostly provided externally and primarily produced from untreated fossil fuels. The implementation of low-emission hydrogen in refining processes might generate large demand for environmentally aware hydrogen and support an accelerated production scale. An envisioned rise in the employment of low-emission hydrogen within refining operations is projected in 2023 [7].

The execution of planned projects, as scheduled, is estimated to generate 1.3 million metric tons of low-emission hydrogen utilized in refineries by 2030. While the use of merchant hydrogen in refining now dominates, it gives an additional path for boosting the availability of low-emission hydrogen in these activities. As per the NZE Scenario, it is estimated that by 2030, about 4 million metric tons of low-emission hydrogen would be manufactured and consumed in refineries. Approximately two-thirds of this hydrogen will be supplied via electrolysis and low-emission energy, while the other third will derive from fossil fuels incorporating CCUS. Notably, about 10% of the stated projects targeted at generating hydrogen by electrolysis for refining purposes have reached the final investment decision (FID) stage [7].

In 2022, the major usage of hydrogen in industrial applications focused on ammonia production, methanol synthesis, and Direct Reduced Iron (DRI) within the iron and steel subsector. Industrial hydrogen production was answerable for producing 680 million metric tons of CO2, representing a 2% increase from the levels noticed in 2021. The worldwide usage of hydrogen in industry observed a 2% rise in 2022, principally spurred by the increasing demand for ammonia, methanol, and DRI. China emerged as the greatest user of hydrogen for industrial reasons, comprising 35% of the total global industrial consumption. However, Europe faced a fall in hydrogen use during 2022 owing to the energy crisis created by Russia's engagement in Ukraine. According to the Net Zero Emissions (NZE) Scenario estimate, hydrogen usage in industry is predicted to climb to 70 million metric tons by 2030, requiring an annual output increase of 4%. The production of low-emission hydrogen in industrial settings in 2022 witnessed a rise to roughly 285 kilotons, reflecting an increase from the 240 kilotons reported in 2021. Despite the publication of the GHR 2022, considerable advancements in hydrogen production via electrolysis have not been recorded. However, the sector has seen the commencement of numerous new projects, poised to augment the predicted low-emission hydrogen production from fossil fuels combining Carbon Capture, Utilization, and Storage (CCUS) by 30%, while electrolysis-based output is anticipated to surge by 50%. Aligning with the objective of reaching net-zero emissions, the industrial sector seeks to create 8.6 million metric tons of low-emission

hydrogen from electrolysis using renewable energy sources and 3.5 million metric tons from fossil fuels employing CCUS within the given period [7].

In 2022, the usage of hydrogen in road transport experienced a huge rise of around 45% in comparison to the previous year, suggesting remarkable expansion in the area. Fuel cell electric vehicles (FCEVs) enjoyed early success in the sales of automobiles, notably in the categories including cars and buses. However, there has been an evident growth in the sales of heavy-duty fuel cell trucks, adding considerably to the total hydrogen use. China's concentration on heavy-duty vehicles and the integration of fuel cell trucks have resulted in a scenario where, despite just 20% of FCEVs being present in China, they account for more than half of the hydrogen utilized in road transport reviewed in Figure 1.2. [7].
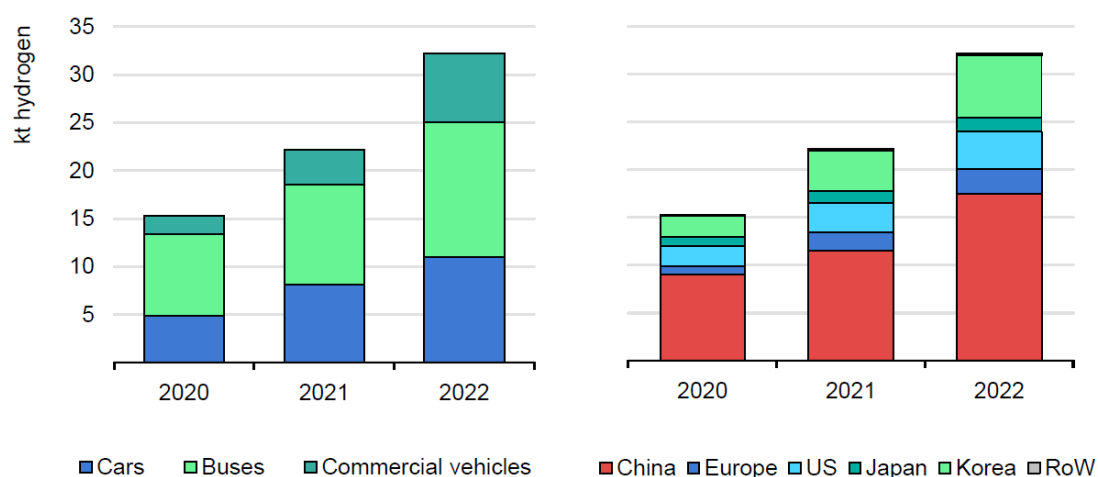
Figure 1.2 Vehiclely and regionly hydrogen consumption, note that (RoW) Rest of World and (US) United States.

The principal domain of hydrogen consumption in the transport industry is projected to stay within road-based applications for the foreseeable future. Nonetheless, rail transport is progressively adding to hydrogen usage via testing and adoptions of hydrogen-powered trains along varied routes. Additionally, the launch of many fuel cell ferries in 2023 is planned to significantly broaden the application of

hydrogen in the transportation sector. Potential developments in the use of synthetic kerosene and direct hydrogen use as an aviation fuel in the following years are projected to enhance the present hydrogen use in the transport sector [7].

In line with the Net Zero Emissions (NZE) Scenario, the estimate for 2030 predicts almost 8 million metric tons (Mt) of direct hydrogen use in transport, largely spread among road transport (50%) and shipping (45%) sectors. South Korea leads as the biggest fuel cell car market internationally, with an inventory topping 32,000 fuel cell autos as of the first half of 2023. Hyundai's Nexo, Toyota's Mirai, SAIC EUNIQ7, Honda Clarity, and BMW have launched small-scale manufacturing of the iX5 Hydrogen fuel cell car in 2022, contributing to the growth of the fuel cell vehicle industry [7].

The market for fuel cell cars is anticipated to change further with the advent of new models. Honda is planned to debut a revolutionary fuel cell car based on its CR-V crossover sports utility vehicle (SUV) in 2024. Additionally, Moroccan start-up NamX has exhibited a prototype fuel cell SUV partially powered by disposable hydrogen capsules, targeting for debut in 2026. Kia, the second-largest automobile maker in Korea, is intending to reveal fuel cell cars beginning from 2027. Moreover, prototype hydrogen cars employing combustion engines have been created by Porsche and Toyota, displaying a multi-technology approach in this arena. However, fuel cell electric cars remain a minority technology, with select corporations focused on battery electric vehicles, highlighted by Volkswagen's initiatives [7].

Expanding the horizon to the light-commercial category, new entrants such as First Hydrogen have began testing for their "Generation I" fuel cell van in 2023, with plans for the production of a second-generation vehicle in succeeding years. RONN Motor Group has revealed its intentions to develop fuel cell delivery vans and medium-duty vehicles. Established automobile major Ford has launched a testing of a fuel cell vehicle in the United Kingdom [7].

The adoption of fuel cell trucks has exceeded the growth rate recorded in light-duty vehicles, representing a notable gain of over 60% in 2022, culminating in a total of more than 7,100 fuel cell trucks by year-end. The bulk of these sales occured in China, which today controls the worldwide market for fuel cell trucks, accounting more than 95% of the overall data. Fuel cell trucks are making inroads beyond China, represented by Hyundai's Xcient, which has amassed 5 million km in Switzerland since 2020, subsequently expanding its operations to Germany, Korea, and New Zealand. Organizations such as Technocarb and CMB.TECH are concentrating on hydrogen combustion, seeking to convert up to 20 vehicles each month. Additionally, there is an ongoing study of hydrogen combustion in automobiles running in dual-fuel mode in New Zealand [7].

In combination with the rise of fuel cell trucks, the stock of fuel cell buses has had a similar expansion pace, recording a 40% increase in 2022 compared to the previous year. A major number, over 85%, of these buses are active in China, followed by Europe, Korea, and the United States. These patterns demonstrate a consistent march towards integrating hydrogen-powered cars into multiple transportation sectors,
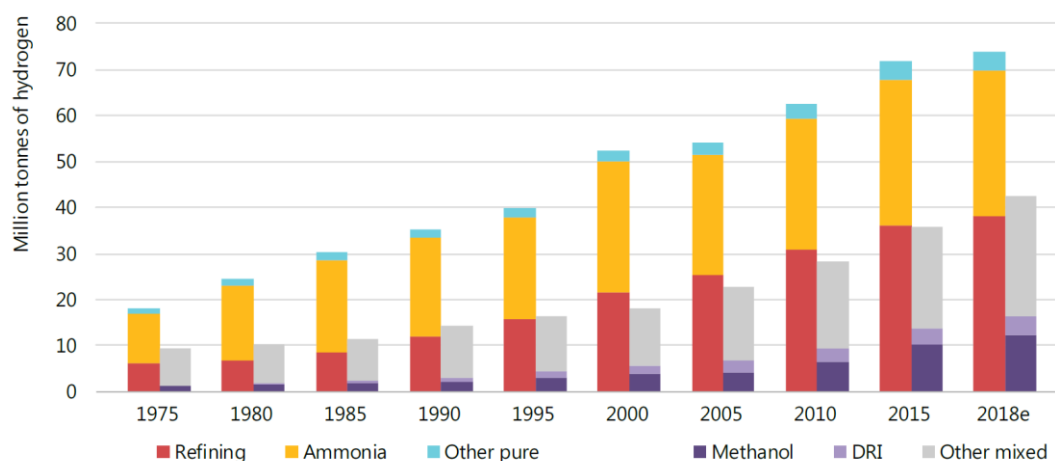
Figure 1.3 since 1975 Globally the hydrogen annual demand

while the speed and degree of adoption varies across different locations and vehicle classifications.

Figure 1.3. explain the Supplying hydrogen to industrial customers has evolved as a substantial worldwide company. The demand for hydrogen has witnessed tremendous development, having climbed by nearly thrice since 1975, showing a steady increasing pattern. The present demand for hydrogen in its pure form is at roughly 70 million tonnes per year (MtH2/yr). Notably, the major source of this hydrogen supply is obtained from fossil fuels, with around 6% of the world natural gas and 2% of the global coal committed to hydrogen generation. Consequently, the process of hydrogen generation accounts for an estimated carbon dioxide (CO2) emission volume of roughly 830 million tonnes per year (MtCO2/yr), an amount similar to the combined CO2 emissions of both Indonesia and the United Kingdom. In terms of energy equivalence, the aggregate yearly hydrogen consumption globally reaches roughly 330 million tonnes of oil equivalent (Mtoe), exceeding the main energy supply of Germany in volume [8].

1.3 Production Of Hydrogen

The production of hydrogen incorporates diverse raw material sources, encompassing both sustainable and non-sustainable origins. Differentiation among various hydrogen types, categorized into distinct color classifications blue, gray, brown, black, and green is based on production technologies, energy sources, and consequential environmental impacts as depicted in Figure 1.4.

Blue hydrogen synthesis entails the reforming by steam of natural gas, decomposing it into hydrogen H_2 and carbon dioxide CO_2, with a notable capture rate of approximately 85% to 95% of the ensuing CO_2, subsequently sequestered underground. Conversely, gray hydrogen, derived from non-renewable fossil fuels like natural gas or coal, shares production similarities with blue hydrogen but does not
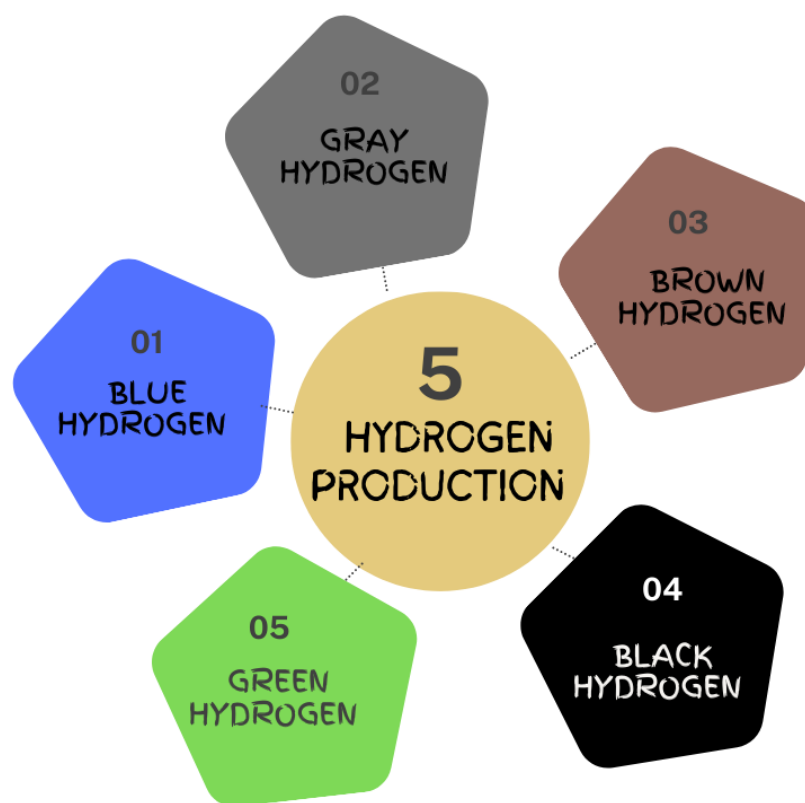
Figure 1.4 The classifications of hydrogen production

capture the resulting CO_2, discharging it directly into the atmosphere. Brown hydrogen currently dominates utilization, produced via the gasification process involving brown coal or methane. Particularly, every unit of brown hydrogen produced emits ten times more carbon dioxide CO_2 into the atmosphere than its production volume. Black hydrogen arises from coal gasification, generating syngas subsequently released into the atmosphere. Conversely, green hydrogen synthesis occurs through electrolysis utilizing renewable water and electricity, involving water decomposition into hydrogen H_2 and oxygen O_2 under the influence of electricity, showcasing zero carbon emissions [9].

1.4 Water Electrolysis

As portrayed in Figure 1.5. Water electrolysis stands as a prominent electrochemical method for green hydrogen production, leveraging electricity in an emission-free technological procedure. The fundamental reaction of water electrolysis, represented by Equation (3), necessitates a theoretical thermodynamic cell voltage of 1.23 V at room temperature to cleave water into hydrogen and oxygen. Presently, four distinct water electrolysis technologies have emerged, differentiated by their electrolyte composition, operational parameters, and the ionic agents employed (such as OH^-, H^+, O^{2-}). These methodologies comprise Alkaline water electrolyzer (AWE), solid oxide water electrolyzer (SOWE), proton exchange membrane water electrolyzer (PEMWE), and Anion Exchange Membrane (AEM) [10].
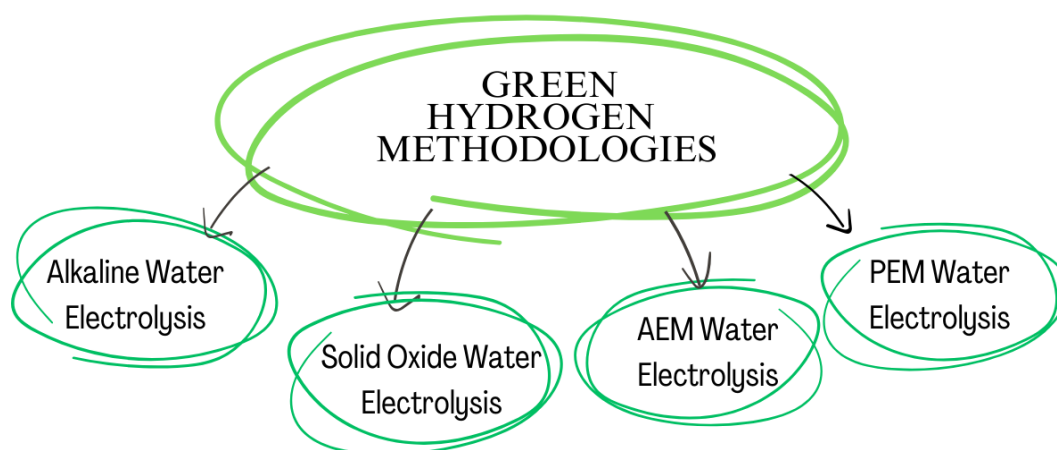
Figure 1.5 Green hydrogen methodologies

1.4.1 Alkaline Water Electrolyzer

The alkaline water electrolyzer occurs within the range of lower temperatures (30–80 ℃), utilizing a concentrated alkaline solution 5M KOH/NaOH. This electrolysis technique employs nickel Ni coated stainless steel electrodes and asbestos/ZrO_2-based diaphragms, functioning as separators. Hydroxyl ions OH^- function as the ionic charge carrier with KOH/NaOH, facilitating the electrochemical reaction through the

permeable structure of the diaphragm. Nevertheless, limitations arise in alkaline water electrolysis due to constrained current densities (0.1– 0.5 A/cm^2), ascribed to moderate OH^- mobility and the use of corrosive KOH electrolytes. Additionally, this procedure yields gases (Hydrogen and Oxygen) with low purity (99.9%) [11].

Figure 1.6 illustrates the main components of the alkaline water electrolysis cell comprise diaphragms/separators, current collectors (gas diffusion layer), separator plates (bipolar plates), and end plates. The electrochemical water division entails two distinct half-cell reactions: the hydrogen evolution reaction (HER) occurring at the cathode and the oxygen evolution reaction (OER) at the anode. Over the electrolysis process, at the cathode, two moles of alkaline solution undergo reduction to result in one mole of hydrogen H_2 and two moles of hydroxyl ions OH^-. The formed H_2 is discharged from the cathodic surface, while the residual hydroxyl ions H_2 migrate through the porous separator to the anode side under the influence of the electric circuit. At the anode, these hydroxyl ions OH^- endure discharge to produce $\frac{1}{2}$ molecule of oxygen O_2 and one molecule of water H_2O.
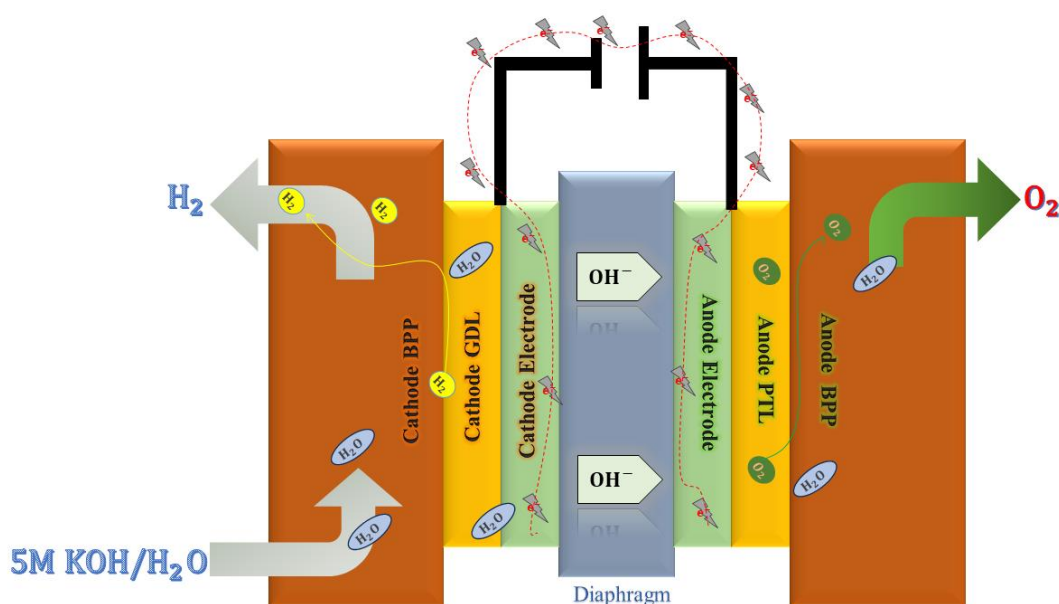
Figure 1.6 Working principle of alkaline water electrolysis

1.4.2   AEM Water Electrolysis

The AEM water electrolysis technology closely matches conventional alkaline water electrolysis with a primary deviation in the substitution of traditional diaphragms (such as asbestos) with an anion exchange membrane, specifically the use of quaternary ammonium ion exchange membranes. Additionally, this substitution in alkaline water electrolysis leads to distinct advantages in AEM water electrolysis. These include the use of cost-effective transition metal catalysts instead of noble metal catalysts and utilizing of distilled water or low-concentration alkaline solution (1M KOH) as an electrolyte as opposed to high-concentration solutions 5M KOH [12].
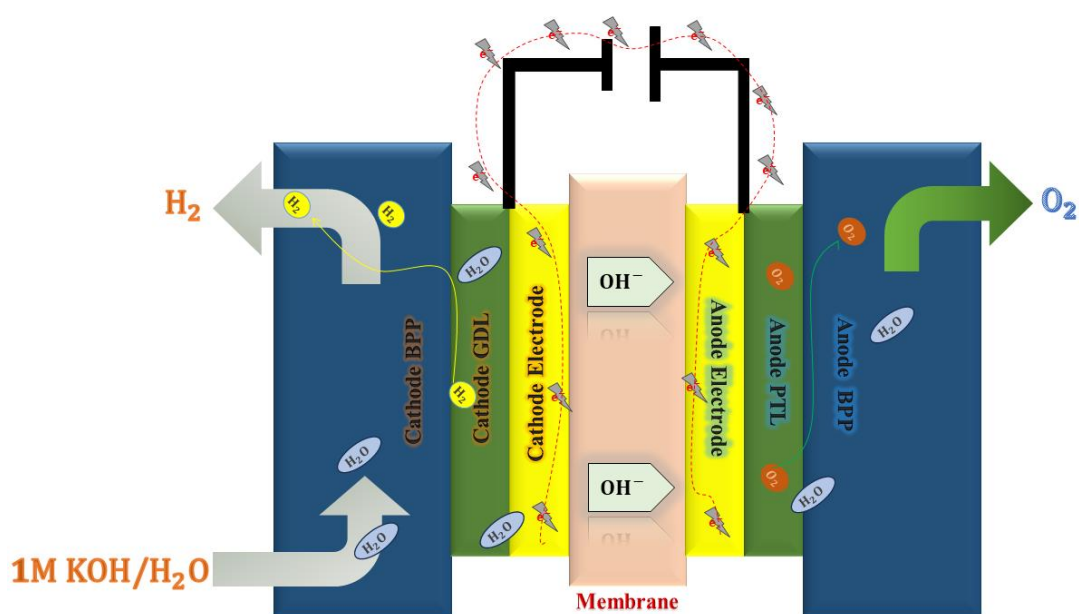
Figure 1.7 Working principle of AEM water electrolysis

The primary components of an AEM water electrolysis cell comprise the membrane (separator), electrode materials, current collectors (gas diffusion layer), separator plates (bipolar plates), and end plates as explained in Figure 1.7. The electrochemical process comprises two half-cell reactions: the hydrogen evolution reaction (HER) and the oxygen evolution reaction (OER). Initially, at the cathode, water molecules undergo reduction, producing hydrogen H_2 and hydroxyl ions OH^- through the addition of two electrons. Hydrogen is discharged from the cathode's

surface, while the hydroxyl ions OH^- traverse the ion exchange membrane toward the anode side, driven by the positive attraction of the anode. Meanwhile, electrons are conveyed through the external circuit to the anode. At the anode, the recombination of hydroxyl ions results in the formation of water molecules and oxygen, while simultaneously releasing oxygen from the anode.

1.4.3 Solid Oxide Water Electrolysis

The solid oxide water electrolysis cell (SOEC) stands as a pivotal electrochemical conversion instrument, converting electrical energy into chemical energy. Operating typically at high temperatures (500–850 ℃), the SOEC utilizes steam-form water, substantially reducing power consumption required for separating water into hydrogen and oxygen. This characteristic enhancement markedly augments energy efficiency and allows simple thermal integration with downstream chemical synthesis processes. Particularly, the solid oxide water electrolysis does not necessitate the use of noble metal electrocatalysts [13].
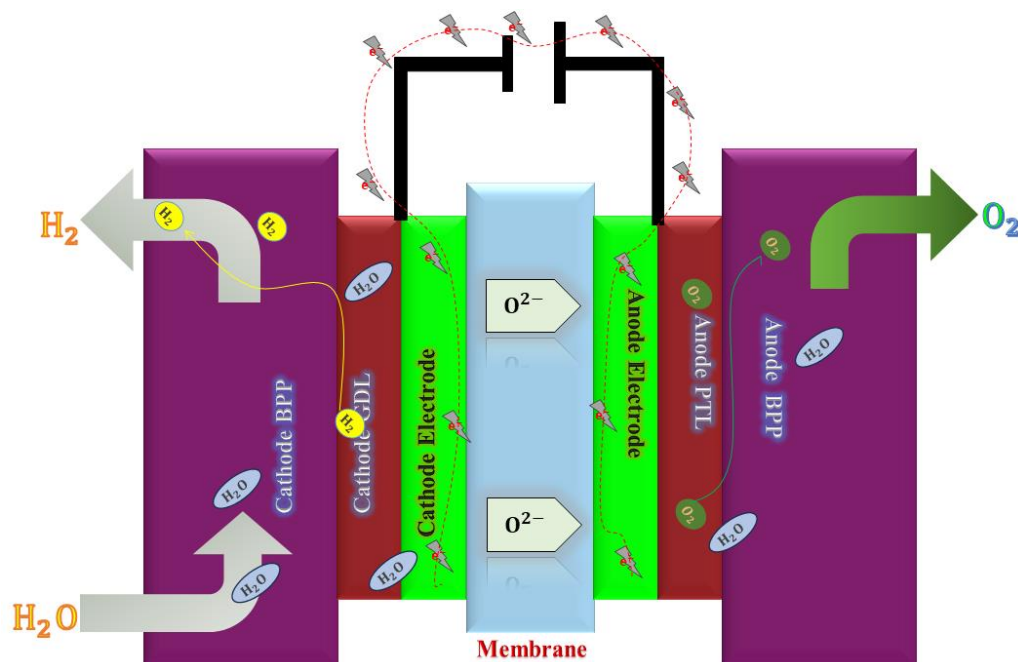
Figure 1.8 Working principle of solid oxide water electrolysis

The SOEC comprises three primary components: two porous electrodes (anode and cathode) and a dense ceramic electrolyte proficient in conducting oxide ions O^{2-} which is illustrated in Figure 1.8. Throughout the solid oxide water electrolysis, initially at the cathode, water molecules undergo reduction, creating hydrogen H_2 and oxide ions O^{2-} through the addition of two electrons. Hydrogen is liberated from the cathode surface, while the residual oxide ions O^{2-} traverse the ion exchange membrane, flowing towards the anode. At the anode, these oxide ions O^{2-} endure further reduction to produce oxygen and electrons. The generated oxygen is released from the anodic surface, while the electrons are conveyed through the external circuit to the cathode side, propelled by the positive attraction of the cathode.

1.4.4   PEM Water Electrolysis

The PEM water electrolysis technology closely follows the design principles of PEM fuel cell technology, employing a sulfonated polymer membrane as the electrolyte. This membrane facilitates the transport of H^+ ions, allowing water to permeate through and facilitating the electrochemical reactions. Operated within lower temperature ranges (30–80 ℃) and higher current densities (1–2 A/cm^2), PEM water electrolysis yields gases (Hydrogen and Oxygen) of extremely high purity (99.999%). Its superior kinetics for the hydrogen evolution reaction, ascribed to the highly active Pt electrode surfaces and lower electrolyte pH, differentiate it from alkaline water electrolysis. However, the implementation of PEM water electrolysis confronts significant cost-related challenges concerning electrode materials, current collectors, and bipolar plates. Throughout the process, water endures electrochemical separation into hydrogen and oxygen. Initially, at the anode, water molecules decompose to produce oxygen O_2, protons H^+, and electrons e^-. Oxygen is released from the anodic surface, while protons move through the proton-conducting membrane to the cathode, where electrons traverse the external circuit. At the cathode, protons and electrons recombine resulting in H_2 gas [13].

The PEMWE is segregated into the cathode and anode by the membrane; every component is made up of a catalyst layer, a gas diffusion layer, and a gas channel as shown in Figure 1.9. Equation (1) illustrates the way water enters the anode channel (ACH) on the anode side and travels through the porous gas diffusion layer (AGDL) and anode catalyst layer (ACL), where it undergoes semi-reactions of oxidation that divide the water into protons, oxygen, and electrons. Protons of hydrogen travel by way of the membrane to reach the cathode catalyst layer (CCL), while electrons move there through an external circuit. Equation (2) describes how hydrogen protons and electrons interact on the cathode side to form hydrogen gas through semi-reactions of a reduction. Equation (3) presents the overall response. Prominent proton exchange membranes include Nafion®, Fumapem®, Flemion®, and Aciplex®, with Nafion® being the most prevalent choice (variants like Nafion® 115, 117, and 212) owing to its high proton conductivity, robust current density, mechanical strength, and chemical stability. Electrode materials for the anode and cathode predominantly constitute noble metal-based electrocatalysts, particularly IrO_2 for the OER and carbon-supported Pt for the HER. Anode and cathode gas diffusion layers are constructed using porous titanium/titanium mesh and carbon cloth, respectively [14-16].
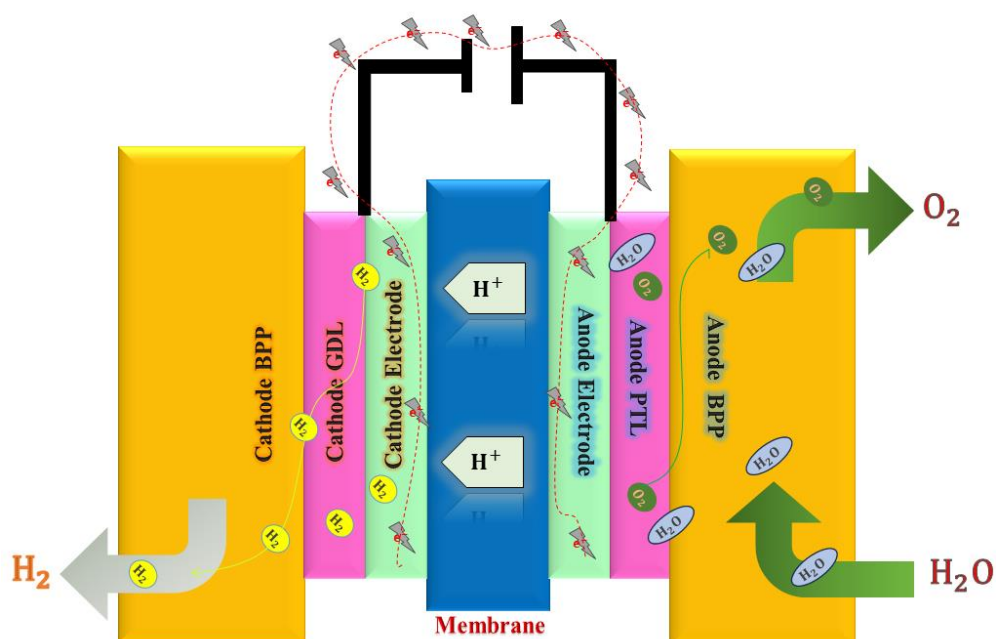
Figure 1.9 Working principle of PEM water electrolysis

$$H_2O_{(liq)} \longrightarrow \frac{1}{2}O_{2(g)} + 2H^+ + 2e^- \qquad (1)$$

$$2H^+ + 2e^- \longrightarrow H_{2(g)} \qquad (2)$$

$$H_2O_{(liq)} + \text{electricity} + \text{heat} \longrightarrow \frac{1}{2}O_{2(g)} + H_2 \qquad (3)$$
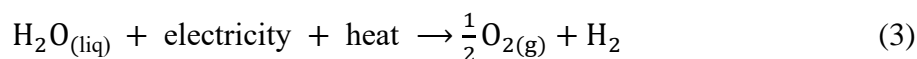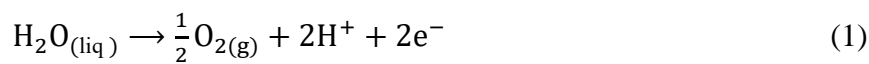
1.4.5   The Importance Of PEMWE

PEM water electrolysis presents numerous advantages over alkaline water electrolysis, including elevated operating current density, enhanced gas purity, increased discharge pressure, and a reduced physical footprint. However, the primary challenge confronting this technology revolves around the component costs, requiring substantive advancements for cost reduction. The membrane, a pivotal component in PEM water electrolyzers, demands considerable innovation and enhancement to augment efficiency, durability, and cost-effectiveness. Similarly, electrocatalysts stand as crucial elements in PEM electrolyzers, necessitating significant innovation due to the predominant use of precious materials like Pt/IrO_2, which pose barriers to both

cost efficiency and scalability. The most considerable cost factor in PEMWE pertains to the stack, comprising about 45% of the overall system cost. Within the stack cost analysis, bipolar plates BPPs account for 53%, superseding other components as shown in Figure 1.10. [17]. The excessive cost attributed to BPPs is anchored in both materials and design aspects. Strategies employing high-purity materials as the foundational structure, along with precision machining for flow field structuring and coating, have been implemented to mitigate the challenges of anodization. The flow field design within bipolar plates markedly influences water electrolysis performance, enabling well-designed flow fields to assure uniform pressure and velocity distributions in the fluid. This design characteristic imbues the stack with heightened operational pressure capabilities and increased current density [18].

Figure 1.10 PEM Electrolyser stack cost out of 45% of the overall system cost

1.5   Literature Review

1.5.1   PEM Fuel Cell Flow Field Design

Proton Exchange Membrane Water Electrolysis (PEMWE) cells and particularly Proton Exchange Membrane Fuel Cells (PEMFC) have a number of similarities. It emphasizes how the advancements in PEMFC technology have contributed to comprehending the requirements and components of PEMWE cells, such as membranes, plates, catalysts, and flow field design. The use of certain designs from PEMFC, adapted for the specific requirements of water electrolysis, is exemplified in the design of Bipolar Plate (BPP) flow fields for PEMWE cells.

Recently, many researchers have performed investigations to increase the performance of bipolar plates (BPPs) as shown in Figure 1.11. (a-b). Wenkai Li et al. [19] introduce an undulating serpentine flow field design that demonstrates an enhancement in promoting oxygen transport and water elimination from micropores also generates a 17.8% higher net maximum power density. Heidary et al. [20] Examines the impact of obstructions within parallel flow field channels of a PEM fuel cell, the blockages enhance oxygen concentration, resulting in higher power and limiting current density, increasing maximal power by 11% and reducing pressure drop. The modified parallel flow field was designed by B.H. Lim et al. accomplished even reactant distribution and pressure reduction from inlet to outlet and the single inlet/outlet configuration provided more homogenous flow distribution [21]. Wang et al. [22] introduce a novel cathode flow design with a sub-channel to optimize water removal and performance in parallel flow-field PEM fuel cells. results show redistributing oxygen and removing excess water downstream, maximum power density, and reducing cathode reactant humidification by 70%. Adding a micro-distributor with parallel flow field was investigated by Haichao Liu et al. Achieved a 22.8% higher maximum power density compared to the conventional design and is only 10.3% lower than the serpentine flow field
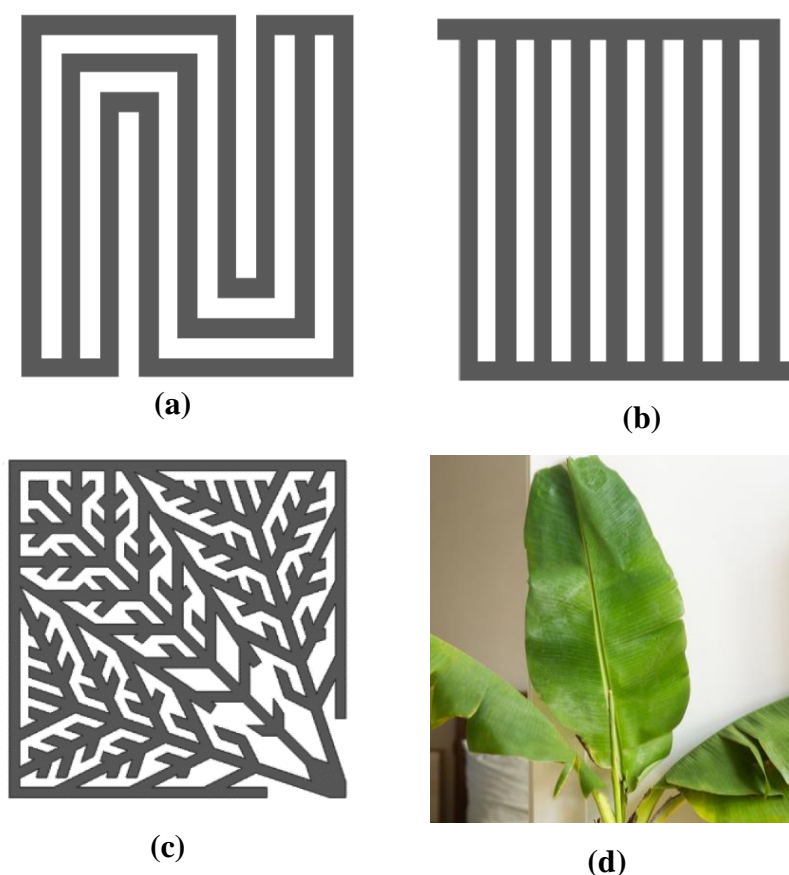
Figure 1.11 Flow field patterns; a) Serpentine flow pattern, b) Parallel flow pattern, c) Murray's law biomimetic flow pattern, d) Exact leaf bio-inspired flow pattern.

[23]. Željko Penga et al.[24] utilized a combination of CFD analysis and neutron imaging to analyze liquid water distribution in a Novel anode flow field which demonstrates its efficacy in reducing mass transport losses and liquid water accumulation. Seyed Ali Atyabi et al. [25] investigated a 3D multiphase CFD model with two distinct flow field designs: sinusoidal and straight-parallel channels. The sinusoidal design had higher maximal velocity, increased pressure drop, boosted uniformity of oxygen mass fraction, and superior performance in managing water and concentration losses. Wang et al. [26] develop a 3D model SOEC with various flow fields. A novel porous material flow field design is proposed, reducing electrolysis voltage demand (0.026 V at 2.5 A/cm^2), increasing efficiency (4.78% at 2.5 A/cm^2),

and improving reaction distribution. Nuttapol Limjeerajarus et al. [27] used a novel hybrid serpentine-interdigitated (HSI) flow field design, providing better power output at a practical operating voltage of around 0.6 V, and 6% increase in net power output by modifying the number of gas inlets/outlets to two and offer more uniform distributions of reactants. Rahimi-Esbo et al. [28] illustrated a parametric investigation of serpentine flow field design The novel one performs effectively, particularly at high current densities, with significant differences in polarization curves observed below 0.5 V and effective water removal. Changing the draft angle, and inner fillet radius by Ah-Reum Kim et al. leads to greater volumetric deformation of the GDM, higher flow resistance, and more uniform oxygen distribution at the reaction zones [29]. Alizadeh et al.[30] İnvstigat the cascade-type serpentine flow fields impact on the performance, polarization, and power curves result in a decrease in current density magnitude due to increased mass fraction losses. Liu et al [31] demonstrate that Combined multi-serpentine flow fields substantially enhance flow uniformity, promote cross-flow under the rib, and lead to more uniform current density distribution, resulting in enhanced output performance and water removal capacity. However, the combined multi-serpentine flow field exhibits inconsistent mass flow rate distribution among its five channels, influencing maximal power density and causing water accumulation in the first sub-channel. Vijayakrishnan et al. [32] Conducted a serpentine-sinuous flow field that offers higher power density compared to the others. İt is 24.44% less power-dense serpentine flow field. In turn reduced pressure drop, better reactant distribution, improved under rib convection, and enhanced water removal. Chowdhury et al. [33] concluded that decreasing channel depth in convergent flow fields raises reactant diffusion and a reduced channel depth gradient between the inlet and combustion results in greater current density and better water management. Havaej et al. [34] studied converging-diverging channel flow pattern on two-phase flow in PEM fuel cells found a 28.2% increase in oxygen mass fraction at the GDL/Channel interface and a 10% enhancement in net output power compared to base cells. Bowen Wang et al. [35] enhance cell performance, particularly at high current densities, and facilitates effective liquid water elimination without obstructing airflow by introducing a novel

dot matrix and sloping baffle flow field plate consisting of diamond-shaped blocks with sloping angles. The 3D Fine mesh flow field studied by Guobin Zhang et al. enhances reactant gas supply and water removal, reducing concentration loss in PEMFC without significant increases in pumping power loss, although it marginally increases ohmic loss in certain scenarios [36].

1.5.2   PEM water electrolyzer flow field design

The efficacy of a PEM electrolyzer system is substantially enhanced through the optimal design of the flow field pattern. Several proposed designs for the flow field in PEM electrolyzers come with their unique advantages and disadvantages. Jianhu et al.[37] conducted numerical simulations to analyze two-phase water/oxygen flow in the anode-side flow field plate of a simplified PEM electrolysis cell. Boosting the mass flow rate of oxygen generation led to locally minimum velocity magnitudes with higher pressure reductions. Olesen et al. [38] investigated the anode flow field of a high-pressure PEM electrolysis cell using a Circular planar interdigitated flow field design that causes maldistribution, with the extent growing with diminished water stoichiometry. Toghyani et al.[39] Modeled PEM electrolyzer with a spiral flow field and investigated the distribution of hydrogen concentration, current density, and pressure. results indicated acceptable uniformity in terms of current density and temperature distribution, with some non-uniformity observed at 90-degree curves and hydrogen concentration decrement due to water stagnation and decreased velocity. Sánchez-Molina et al. [40] demonstrate the feasibility of using additive manufacturing (AM) for producing metal bipolar plates in PEM electrolyzers. AM offers the advantage of rapid, cost-effective production and the potential for designing more efficient flow distribution channels. In a comparable analysis that Jianhu made, Safiye Nur et al. [41] That oxygen volume fraction is highest at the center of the anode flow field plate and increases from the channel inlet to the outflow, with a commensurate increase in pressure decrease as oxygen production rises. Increasing the number of channels from 4 to 14 contributed to a decrease in pressure reduction. The velocity distribution was found to be non-uniform, with high velocity at the inlet and outlet

manifolds and decreased velocity in the midsection of the flow field region. Rui Lin et al.[42] investigate Three distinct flow field structures were analyzed through 3D simulations and their impact on electrolyzer performance under diverse operating conditions. The findings demonstrated that the choice of flow field design substantially influences electrolyzer performance, with the parallel flow field, operating at 60℃ and 0.1 bar anode pressure.

1.5.3 Bio-inspired flow field design

Bio-inspired design has already demonstrated its disruptive power in generating numerous products and societal impacts in a relatively brief period. However, the lack of organized connections between academia, industry, and translational apparatus has limited its extensive impact, and systematic investment and education for academic researchers are seen as important factors to activate the field's full potential as shown in Figure 1.11. (c-d). The Convergence Accelerator approach is anticipated to have a major effect on advancing bio-inspired design. Recently has been used to enhance the efficacy of the PEMWE. Roshandel et al. [43] compared conventional designs with bio-inspired patterns. The results indicated that the bio-inspired patterns exhibited more homogenous species and velocity distribution, leading to enhanced fuel cell performance and achieved higher power density than parallel and serpentine flow channels by up to 56% and 26%. Ruan et al. [44] Introduced a novel biomimetic flow channel design for PEMFCs, divulging that the biomimetic flow channel enhances power output, assures a more uniform distribution of reaction gases, and facilitates the removal of excess reaction products in PEMFCs. A different approach novel bio-inspired lung-shaped bipolar plate by Asadzade et al. which demonstrated minimal pressure loss, uniform reactant distribution, and appropriate fluid velocity, while avoiding static points that could obstruct gas diffusion layer apertures [45]. Dong-Hui et al. [46] introduced inspiration from bionics, fractal theory, and Murray's law to reduce friction forces in reactant flow. Shows that the Intersectant flow field design offers advantages such as more uniform reactant distribution, effective exhaust of reaction products, higher power, and current density compared to the serpentine flow

field. Trogadas et al. [47] present a nature-inspired, lung-inspired fractal flow field with 5 generations that offers the best performance at high current densities due to more uniform reactant distribution across the catalyst layer. Ouellette et al. [48] performance of different flow fields for anodes and cathodes in a direct methanol fuel cell (DMFC) was examined, comparing serpentine, bio-inspired interdigitated, and non-interdigitated designs, indicating that the serpentine flow field performed best on the anode, and the interdigitated flow field excelled on the cathode due to enhanced under-rib convection. Kang et al. [49] Aimed to investigate leaf vein-inspired flow fields on bipolar plates. results showed that the ginkgo flow field, simulating leaf veins, exhibited a power density 7% lower than the serpentine flow field and 40% higher than the parallel flow field, and superior water removal capability compared to the parallel and net leaf flow fields. Longer unit channels in the ginkgo pattern enhanced water removal. Dong et al. [50] introduced A novel bio-inspired flow field design based on principles of bio-inspiration and Murray's law and numerically simulated. The results demonstrated that the bio-inspired flow field substantially enhanced the uniformity of reaction gas distribution, reduced pressure loss, and increased the maximal power output of PEM fuel cells by 114% compared to the parallel flow field.

1.6 The significance of the project

$$H_2O_{(liq)} + electricity + \xrightarrow{HEAT} \frac{1}{2}O_{2(g)} + H_2$$

$$CO_2 + H_2O \xrightarrow{LIGHT} C_6H_{12}O_6 + O_2$$
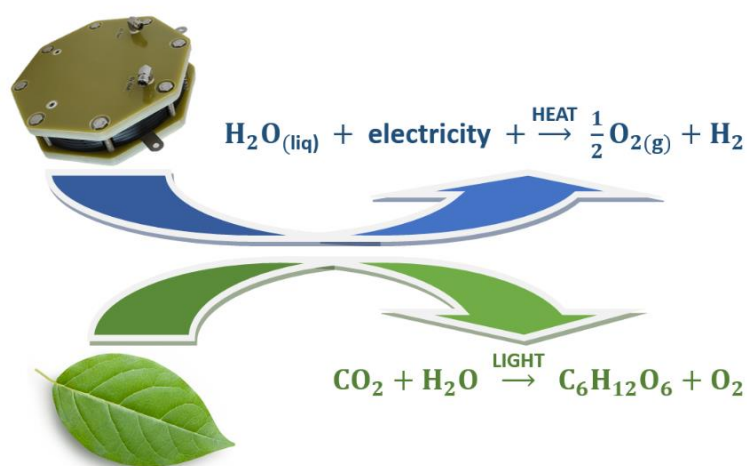
Figure 1.12 The work principle and function similarity between the leaf and the PEMWE

In spite of the extensive corpus of research dedicated to the modeling of Proton Exchange Membrane (PEM) electrolysis, a substantial volume of academic study has been dedicated to the investigation of flow field patterns within Bipolar Plates (BPs) for Proton Exchange Membrane Fuel Cells (PEMFC). A subset of these investigations have attempted to analyze the flow field patterns in PEMFC with a bio-inspired paradigm; however, it is noticeable that none of these studies have incorporated precise bio-geometric considerations. Conversely, the literature exhibits an absence of numerical investigations into the flow field dynamics of PEM water electrolyzers. To the best of our knowledge, the exploration of exact leaf bio-inspired flow field patterns for PEM water electrolyzers remains an uncharted domain in the extant corpus of research. In summary, the unique contributions of the current study relative to comparable works appear in the formulation of an original three-dimensional model utilizing a finite volume approach. Furthermore, the investigation includes the modeling of traditional flow field patterns, specifically those characterized by parallel, point, and serpentine configurations. A detailed comparison transpires, evaluating diverse flow field types through the acquisition and assessment of their pressure, velocity, and mixture distribution profiles. Additionally, the research presents and models an innovative bio-inspired flow field design, drawing inspiration from extant natural specimens such as the veins of plants and foliage, incorporating precise geometric accuracy in the modeling process and Leaf has almost a similar function that electrolyzer has and their working principles are very near to each other as shown in Figure 1.12. The CO_2 and water go through the vines and with the assistance of solar energy It produces glucose and O_2 On the other hand in PEMWE the water passes through channels and with the aid of electrical energy It produces H_2 and O_2.

CHAPTER 2

MODELING

2.1 Modeling Definition

This work employs a single-phase-domain approach to implement the nonlinear differential equations for a three-dimensional single-half-cell PEMWE. The finite element method is used to model the conservation equations for electrochemical reactions that must be solved simultaneously across seven regions of the cell, including the anode and cathode catalyst layer, GDLs, anode channel, and membrane (schematic diagram of a typical PEMWE is shown in Figure 2.1.
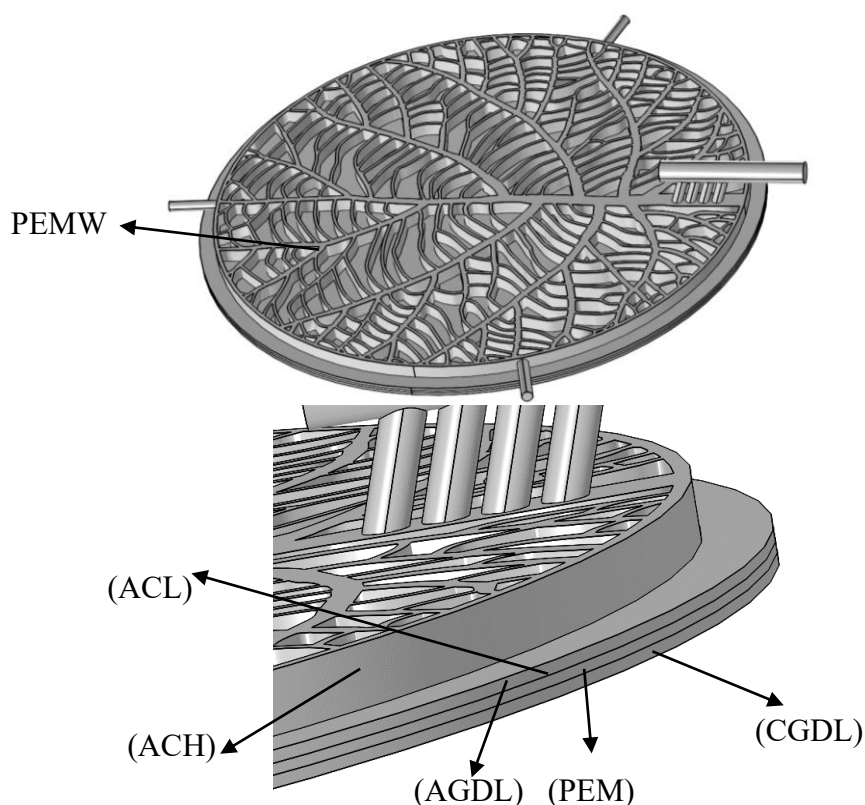
Figure 2.1 A typical PEM water electrolyzer that consists of (ACL, CCL, ACH, AGDL, CGDL, and PEM).

A computational fluid dynamics (CFD) 3D model for utilizing numerical model of PEMWE using COMSOL Multiphysics, is constructed. The mesh independence of the results is verified to certify that the results are independent of the mesh which shown in Figure 2.4. The geometry parameters, physical parameters, and operating conditions for the PEMWE are shown in Table 2.1. and Tables 2.2. Several leaves have been chosen from nature depending on their shapes and their performance which come from the Maximal efficiency of water transport in leaves which in turn related to vein density and the length of the hydraulic pathway through the mesophyll [51 - 52]. With the help of computational Software, we could export the exact leaf vein geometry which gives our study the uniqueness from the rest of the research. After that, we do a mesh with focusing on the carves and the interface boundaries as illustrated in Figure 2.2.

Table 2.1 Geometrical parameters of the leaf bio-inspired flow fields.

Name	Side	Material	Value	Unit	Source
Cell radius			0.0215	m	-
Cell Area			0.001385	m^2	-
GDL thickness	Anode	Ti mesh	2E−4	m	[53]
	Cathode	Ti mesh			[53]
CL thickness	Anode	Iridium dioxide (IrO_2)	1E−5	m	[54]
	Cathode	platinum with carbon (Pt/C)			[54]
Membrane thickness		Nafion® 117	1.78E−4	m	[53]
Channel thickness			0.001	m	[53] [55]

Table 2.2 Operational parameters of the leaf bio-inspired flow fields

Name	no	Value	Unit	Source
Cell temperature		328.15	K	-
Reference temperature		298.15	K	[53]
Reference pressure		1.01E+05	Pa	[53],[55]
Mass flow rate		1.9379E−6	kg/s	[56]
Current density		0.2 to 1.5	A/cm^2	-

Water stoichiometry ratio	1	-	[56]
Membrane conductivity	20.22	S/m	[57]
Stoichiometric coefficient of H_2	0.5	$kmol_{H_2}/kmol_{e^-}$	[55]
Stoichiometric coefficient of H_2O	0.5	$kmol_{H_2O}/kmol_{e^-}$	[55]
Stoichiometric coefficient of O_2	-0.25	$kmol_{O_2}/kmol_{e^-}$	[55]
Number of participating electrons	1	1	[55]
PTL conductivity	3.78E7	S/m	[55]
PTL permeability	1E−11	m^2	[53]
PTL porosity	0.72	-	[53]

Table 2.3 (continue to 2.2) Operational parameters of the leaf bio-inspired flow fields

Name	no	Value	Unit	Source
Anodic transfer coefficient		0.5	-	[59],[53]
Active Specific surface area		10000	m^2/m^3	-
Reference exchange current density, anode	*1*	0.0075	A/m^2	[59]
	2	5E−8	A/m^2	[53]
	3	0.01	A/m^2	[58]
Reference exchange current density, cathode	*1*	120	A/m^2	[59]
	2	10	A/m^2	[53]
	3	2900	A/m^2	[58]
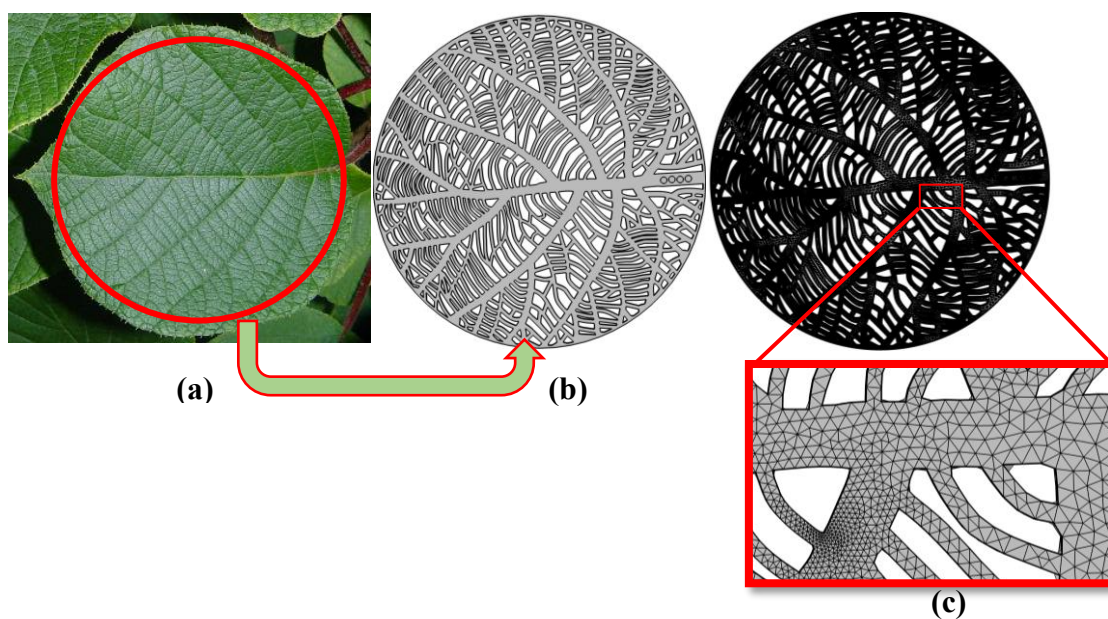
Figure 2.2 Model process before the simulation; a) the leaf selection (depending on their shapes and hydraulic pathway [51 - 52]), b) Design and extract the exact vein geometry, and c) Mesh the model.

2.2 Modeling Assumption

The modeling studies focus on optimizing the anode channel patterns using the leaf-bio inspired flow-field of five leaf vein patterns (Acalypha Hispida leaf, Kiwi leaf, Nelumbo Nucifera leaf, Soybeans, and Victoria Amazonica Water Lily leaf) shown in Table 2.4. with their model names to improve PEMWE performance. A three traditional flow field pattern Table 2.6. was modeled and simulated to clearly see the result of this study through the comparison between them. A few presumptions are made in this model in order to avoid confusion and maintain consistency in a fruitful compromise. It is assumed that the model is operating in a steady state. Laminar flow has one or more inlets and one or more outlets, and it is incompressible. Isothermal Newtonian fluid that disregards gravity Potential and kinetic energy changes are ignored, one bar of anode pressure is present. The gas mixture is subjected to ideal gas behavior. There has been a disregard for the contact resistance between different layers. It is assumed that the GDL, catalyst layer, and membrane are homogeneous and isotropic.

Table 2.4 The modeled leaf bio-inspired flow pattern model; a) L1U Soybeans b) L2V Victoria Amazonica Water Lily, c) L3N nelumbo nucifera, d) L4K Kiwi, e) L5A Acalypha Hispida.

No	Name	Real Leaf	Modeled leaf
(a)	L1U		
(b)	L2V		
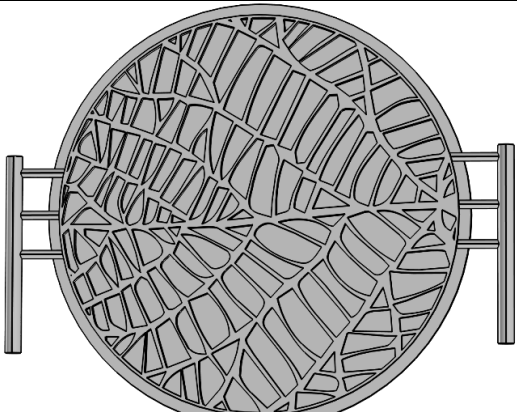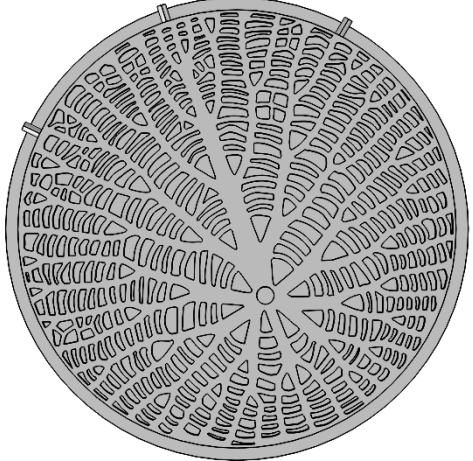
Table 2.5 (continue to 2.4) The modeled leaf bio-inspired flow pattern model; a) L1U Soybeans b) L2V Victoria Amazonica Water Lily, c) L3N nelumbo nucifera, d) L4K Kiwi, e) L5A Acalypha Hispida.

No	Name	Real Leaf	Modeled leaf
(c)	L3N		
(d)	L4K		
(e)	L5A		
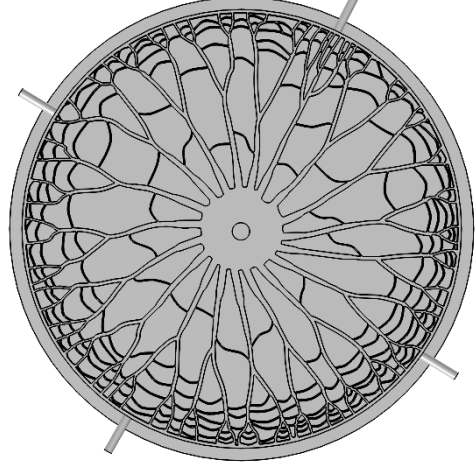
Table 2.6 The modeled traditional flow pattern model; a) PR6 Parallel b) PO7 point, c) SR8 Serpentine.

(a)	(b)	(c)
PR6	**PO7**	**SR8**
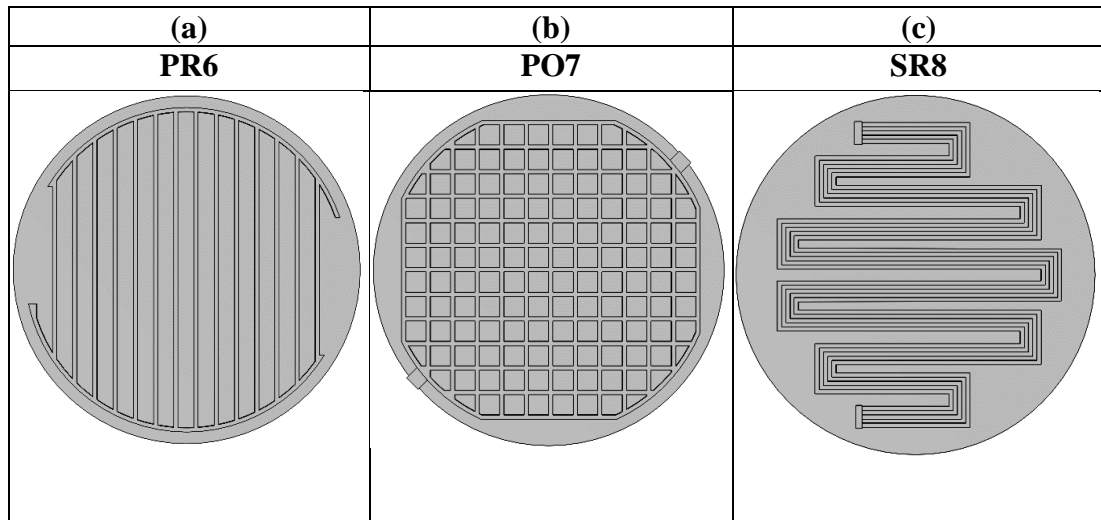
2.3   Governing Equation And Numerical Methods

Conservation of mass - In Flow fluid model part a free and porous media applied with enable porous media domains and neglect the gravity effect. for zero velocity condition at the wall, mass exchange occurs at Porous Medium calculated by equation (4):

$$\rho \nabla \cdot \mathbf{ua} = Q_{\mathrm{m}} \tag{4}$$

where u is the mixture velocity vector (m/s) , ρ is the mixture density (kg/m^3), Q_{m} is the source term or mass source [kg/(m^3.s)]. For the inside channel fluid properties, Q_{m} is zero using equation (5):

$$\rho \nabla \cdot \mathbf{ua} = 0 \tag{5}$$

conservation of momentum - the momentum conservation applied for the channel fluid and Porous Medium GDL as shown in equations (6-9) respectively:

$$\rho(\mathbf{ua} \cdot \nabla)\mathbf{ua} = \nabla \cdot [-p\mathbf{aIK}] + \mathbf{F} \tag{6}$$

$$\mathbf{K} = \mu(\nabla \mathbf{ua} + (\nabla \mathbf{ua})^{\top}) \tag{7}$$

$$\frac{1}{\epsilon_p}\rho(\mathbf{ua}\cdot\nabla)\mathbf{ua}\frac{1}{\epsilon_p} = \nabla\cdot[-p\mathbf{I}+\mathbf{K}] - \left(\mu\kappa^{-1}+\beta p|\mathbf{ua}|+\frac{Q_m}{\epsilon_p^2}\right)\mathbf{ua}+\mathbf{F} \tag{8}$$

$$\mathbf{K} = \mu\frac{1}{\epsilon_p}(\nabla\mathbf{ua}+(\nabla\mathbf{ua})^\top)-\frac{2}{3}\mu\frac{1}{\epsilon_p}(\nabla\cdot\mathbf{ua})\mathbf{I} \tag{9}$$

Where p is the pressure (N/m^2), μ is the dynamic viscosity of the mixture [kg/(m.s)], $\mathbf{K}$ is the viscous stress tensor Pa , $\mathbf{F}$ is the volume force vector (N/m^3) and, $\top$ is the absolute temperature K , Where ϵ_p is the GDL porosity, κ the permeability of the GDL (m^2), and β drag force coefficient. which is assumed to be zero.

Mass Diffusion (Maxwell–Stefan) - In electrochemical model part PEMWE selected including H_2O species, gas phase diffusion, and $H_2O_{(liq)}$ in reaction stoichiometry. In order to solve for the fluxes of each species in terms of mass fraction, The whole computational domain multispecies mass transports described by the Maxwell–Stefan equation (diffusion equation) (10-14) respectively:

$$\nabla\cdot\mathbf{j}_i+\rho(\mathbf{u}\cdot\nabla)\omega_i = R_{i,\,\text{total}} \tag{10}$$

$$\mathbf{j}_i = -\rho\omega_i\sum_k \widetilde{D}_{ik,\,\text{eff}}\,\mathbf{d}_k \tag{11}$$

$$\mathbf{d}_k = \nabla x_k+\frac{1}{p_A}[(x_k-\omega_k)\nabla p_A], x_k = \frac{\omega_k}{M_k}M_n \tag{12}$$

$$p_i = x_i p_A \tag{13}$$

$$M_n = \left(\sum_i \frac{\omega_i}{M_i}\right)^{-1} \tag{14}$$

Where $\mathbf{u}$ is the mass averaged velocity of the mixture (m/s) , $\mathbf{j}_i$ is the mass flux relative to the mass-averaged velocity [kg/(m^2.s)] , ω_i is the mass fraction (1), $R_{i,\,\text{total}}$ is the rate expression describing its production or Consumption [kg/(m^3.s)] , $\widetilde{D}_{ik,\,\text{eff}}$ is the multicomponent Fick diffusivities (m^2/s) , $\mathbf{d}_k$ is the diffusional driving force (1/m) acting on species k, x_k mole fraction (1), p_A is the total anode pressure (Pa), M_n mean molar mass (kg/mol) , and p_i partial pressures (Pa).

Electronic and Protonic charge conservation equation - The current continuity equations are obtained by using Ohm's law for the membrane and electrode shown in equations (15-18) respectively:

$$\nabla \cdot \mathbf{i}_I = i_{v,\,total} \tag{15}$$

$$\mathbf{i}_I = -\sigma_{l,eff}\nabla\phi_l \tag{16}$$

$$\nabla \cdot \mathbf{i}_s = -i_{v,\,total} \tag{17}$$

$$\mathbf{i}_s = -\sigma_s\nabla\phi_s \tag{18}$$

The ϕ_l and ϕ_s are Electrolyte and Electronic Phase node solves for the electric potential V respectively as dependent variable. Where $\mathbf{i}_I$ is the current density in the phase (A/m^2), $\sigma_{l,eff}$ and σ_s are the effective electrolyte and electronic conductivity (S/m) respectively, and $i_{v,\,total}$ is the sum of a volumetric current density (A/m^3). The source terms in the electron and proton transport equations result from the electrochemical reaction, which occurs only in the catalyst layers of anode and cathode sides.

Constitutive relations - In this model Nernst equation used for equilibrium potential with local current density from kinetics expression type and the source terms in both species and charge equations are related to the current density of the charge transfer electrode reaction i_{loc} (A/m^2) which was calculated by using a simplified Butler-Volmer equation, mass action law type exchange current density, and Stefan velocity (19-26):

$$\eta = E_{ct} - E_{eq} \tag{19}$$

$$E_{ct} = \phi_s - \phi_l \tag{20}$$

$$i_v = a_v i_{loc} \tag{21}$$

$$R_i = -\frac{M_i v_i i_v}{nF} \tag{22}$$

Where, η is the activation overpotential (V), E_{eq} denotes the equilibrium potential (V), a_v is the active specific surface area (m^2/m^3), M_i is the species molar mass (kg/mol), F is the Faraday constant (coulomb/mol), n is the number of participating electrons (1), v_i stoichiometric coefficient (1).

$$\mathbf{n} \cdot \mathbf{i}_I = d_{gde}\left(\sum_m i_{v,m} + i_{v,dl}\right) \tag{23}$$

$$\mathbf{n} \cdot \mathbf{i}_s = -d_{gde}\left(\sum_m i_{v,m} + i_{v,dl}\right) \tag{24}$$

$$-\mathbf{n} \cdot (\mathbf{j}_i + \rho u_s \omega_i \mathbf{n}) = d_{gde} \sum_m R_{i,m} \tag{25}$$

$$\rho u_s = \mathbf{n} \cdot \sum_i (\mathbf{j}_i + \rho u_s \omega_i \mathbf{n}) \tag{26}$$

Where $\mathbf{n}$ is the unit normal pointing out of the fluid domain, $\mathbf{i}_I$ and $\mathbf{i}_s$ are the current density vector in the electrolyte and electrode (A/m^2) respectively, d_{gde} is the electrode thickness (m), $\mathbf{j}_i$ denotes the mass flux $[kg/(m^2.s)]$ of species i relative to the mixture (typically due to diffusion), u_s referred to as the Stefan velocity (m/s).

2.4 Boundary Conditions

Inlet - With 0.9 mole fraction of $H_2O_{(liq)}$ as an initial condition, and the $\dot{m}$ mass flow rate (kg/s) inlet boundary condition calculated by equations (27,28) [56]:

$$-\int_{\partial\Omega} \rho(\mathbf{ua} \cdot \mathbf{n})d_{bc}dS = m \tag{27}$$

$$\dot{m} = \lambda M_{H_2O}\left(\frac{J}{2FA}\right) \tag{28}$$

Where d_{bc} is the boundary thickness m normal to the fluid-flow domain (only present in the 2D Cartesian axis system), λ is the stoichiometric ratio of feed water, M_{H_2O} is the molar weight of water (g/mol), J is the current density (A/cm^2), and A is the active area (m^2).

Outlet – in the PEMWE model part Including gas phase diffusion in gas diffusion layer using D_{ik} binary diffusivities (m^2/s). The outlet condition calculated by equations (29,30):

$$\mathbf{n} \cdot \rho \omega_i \sum_k \widetilde{D}_{ik,\,\text{eff}} \, \mathbf{d}_k = 0 \tag{29}$$

$$D_{ik,\,\text{eff}} = \epsilon_g 1.5 D_{ik} \tag{30}$$

On other hand, In Flow fluid model part a free and porous media Applies the Static Pressure boundary condition at the outlet, With normal flow. Where static pressure $\widehat{p_0}$ donated by "$\widehat{}$" due suppress backflow condition (31,32):

$$(\mathbf{n})^\top [-pa\mathbf{I} + \mathbf{K}]\mathbf{n} = -\widehat{p_0} \tag{31}$$

$$\widehat{p_0} \le p_0, \, \text{ua} \cdot \mathbf{t} = 0 \tag{32}$$

Wall - The Symmetry boundary condition is applied on the GDL side walls and the no-slip boundary condition apply to the rest walls (33,34):

$$\text{ua} \cdot \mathbf{n} = 0 \tag{33}$$

$$K_\mathbf{n} - (K_\mathbf{n} \cdot \mathbf{n})\mathbf{n} = \mathbf{0}, \mathbf{K_n} = \mathbf{Kn} \tag{34}$$

Current density- For electrode current density, $i_{s,\,\text{average}}$ Inward current density (A/m^2) taken as an average from 2000 to 15000 (A/m^2) integrated over a mesh Titanium (35):

$$-\int_{\partial\Omega} \mathbf{i}_S \cdot \mathbf{ndS} = i_{s,\,\text{average}} \int_{\partial\Omega} \mathrm{dS} \tag{35}$$

2.5 Validation

Upadhyay et al. [54] used 3D computational fluid dynamics simulations to examine the performance of a proton exchange membrane (PEM) water electrolyzer, with the obtained results validated against experimental data, which has been combined with this study. Figure 2.3 compares the polarization curve obtained through

Upadhyay's investigation to the polarization curve projected by the current numerical model. These comparative evaluations were carried out under specific operating conditions, with a pressure of 1 bar and temperatures kept at 328.15 K. The numerical model's predictions closely match the results of Upadhyay's study, confirming the current simulation model's reliability and accuracy.
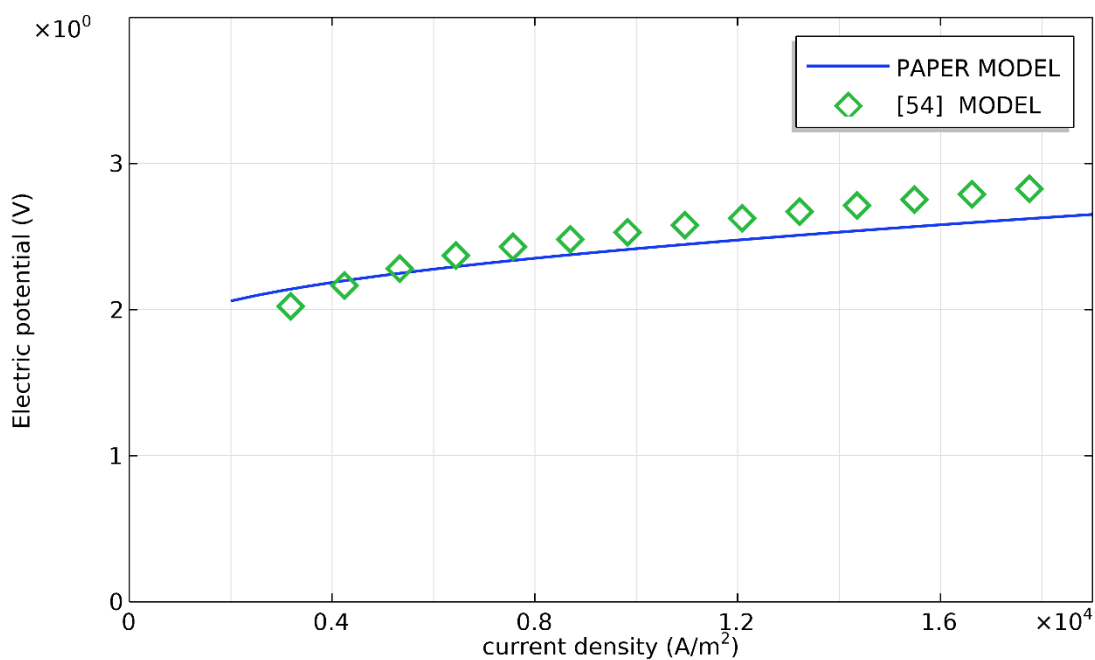
Figure 2.3 The model validation the using the comparison between the polarization curves of this model and Upadhyay et al. [54] study.
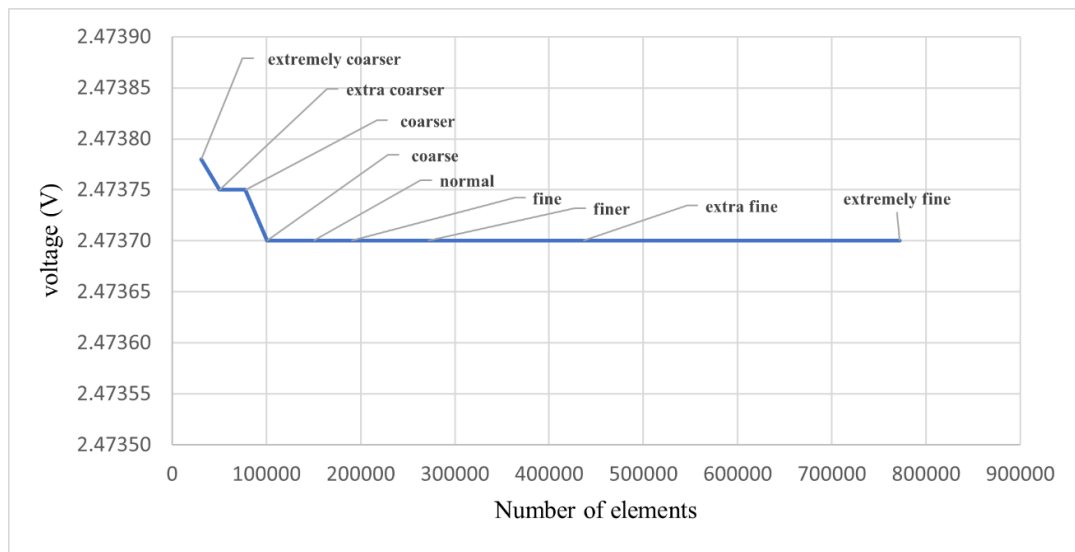
Figure 2.4 Mesh independence study.

CHAPTER 3

RESULT AND DISCUSSION

3.1 Polarization Curve

Figure 3.1 Polarization curves of the all models; traditional models (PR6 Parallel, PO7 point, SR8 Serpentine) and leaf bio-inspired models (L1U Soybeans, L2V Victoria Amazonica Water Lily, L3N nelumbo nucifera, L4K Kiwi, L5A Acalypha Hispida).

The investigation of PEM water electrolyzer characteristics involves an examination utilizing the polarization curve, which correlates the electrolyzer's voltage with its current density. This curve serves as a primary tool for characterization and comparative performance analysis among different electrolyzer types. In this study, five-leaf bio-inspired models were compared alongside three traditional models across a specified range. As depicted in Figure 3.1. The leaf bio-inspired models, on average, exhibit lower polarization curves in contrast to their traditional model counterparts. Notably, the L2V, L4K, and L5A models demonstrate the most favorable performance in terms of polarization curves, respectively. For instance, in the case of L2V, an

increase in voltage from 1.9751 to 2.5173 V results in a corresponding variation in current density ranging from 200 to 15000 A/m^2 , observed at an operating temperature of 328.15 K and a pressure of 1 bar with variable mass flow rate controlled by equation (28).

3.2 Pressure

The pressure distribution significantly impacts the performance of Proton Exchange Membrane Water Electrolysis (PEMWE) cells. A substantial pressure drop across the cell augments water management capabilities but complicates reactant distribution within the cell. Therefore, optimizing the pressure distribution to maintain high water removal capability while minimizing pressure drop is crucial. Figure 3.3. and Figure 3.4. depict the pressure drop along the anode compartment and the anode GDL at a specific current density of 15000 A/m^2. Additionally, Figure 3.2. illustrates pressure drop profiles across models, demonstrating that L2V exhibits the lowest pressure drop among all models. Notably, traditional models exhibit significantly higher pressure drops, particularly the multi-serpentine design reaching 476.48 Pa Figure 3.3. (c), compared to leaf bio-inspired models with a notably lower average inlet-to-outlet path length. Longer paths in traditional designs contribute to increased pressure drop, warranting separate pressure scales for comparison.
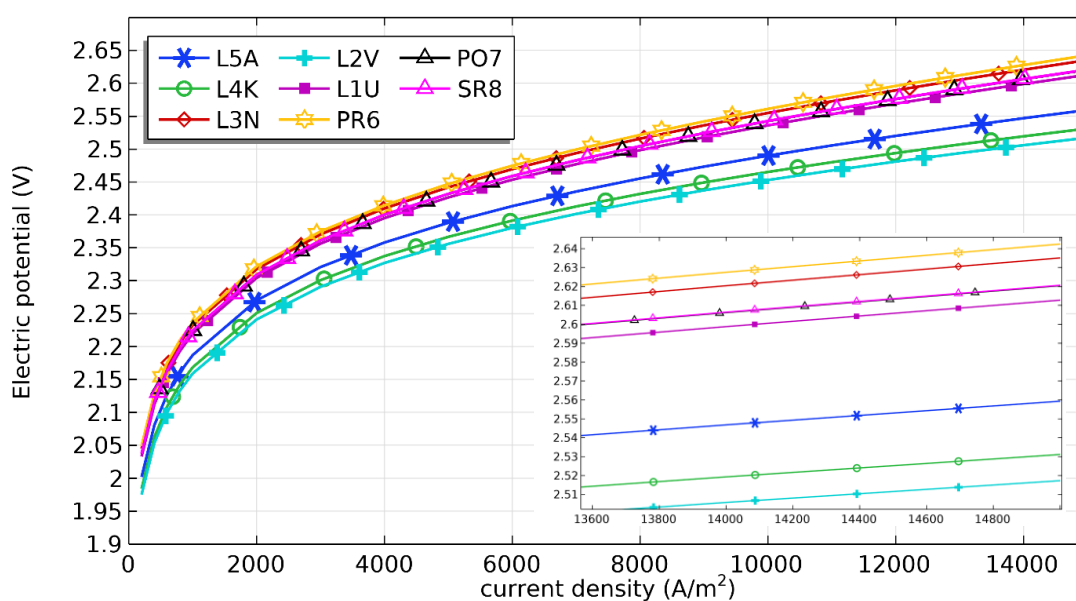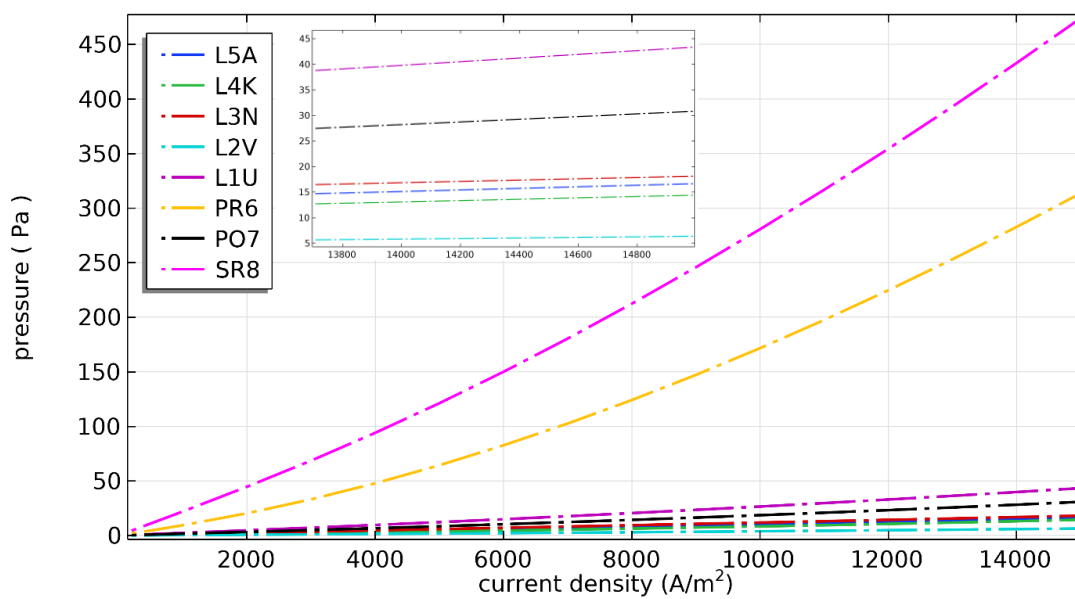
Figure 3.2 Pressure Drop of the all models; traditional models (PR6 Parallel, PO7 point, SR8 Serpentine) and leaf bio-inspired models (L1U Soybeans, L2V Victoria Amazonica Water Lily, L3N nelumbo nucifera, L4K Kiwi, L5A Acalypha Hispida).
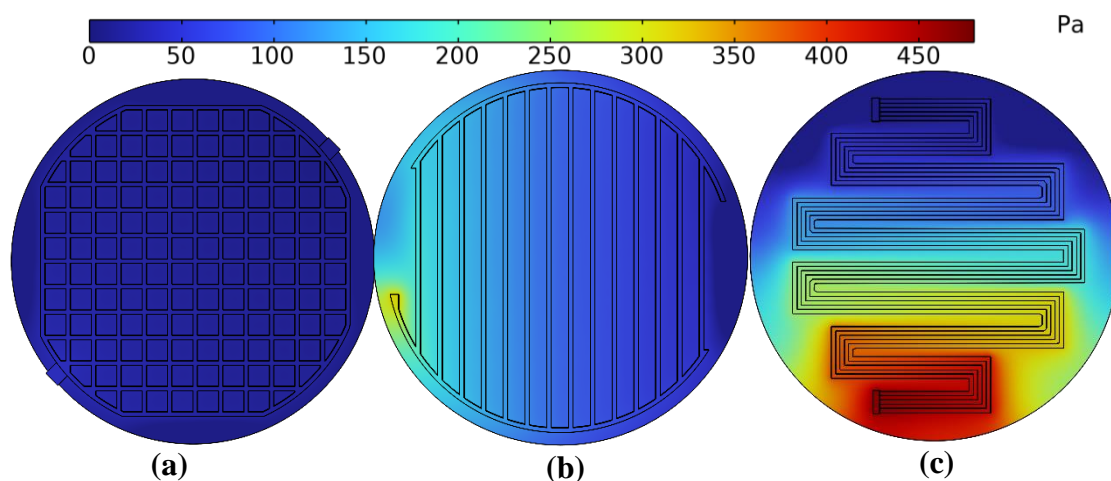
Figure 3.4 Pressure distribution of the traditional models with pressure scale from 0 to 480 Pa ; (a) PO7 point, (b) PR6 Parallel, (c) SR8 Serpentine.
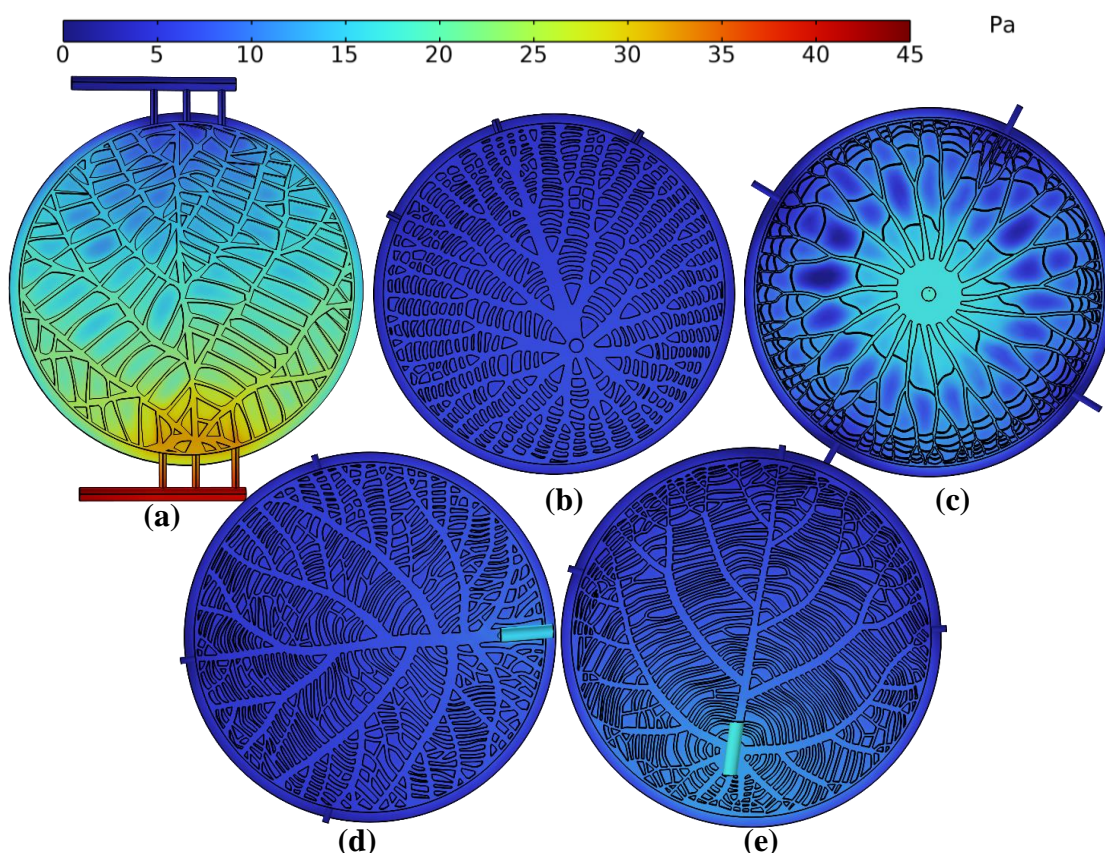
Figure 3.3 Pressure distribution of the leaf bio-inspired models with one pressure scale from 0 to 45 Pa ; (a) L1U Soybeans, (b) L2V Victoria Amazonica Water Lily, (c) L3N nelumbo nucifera, (d) L4K Kiwi, (e) L5A Acalypha Hispid
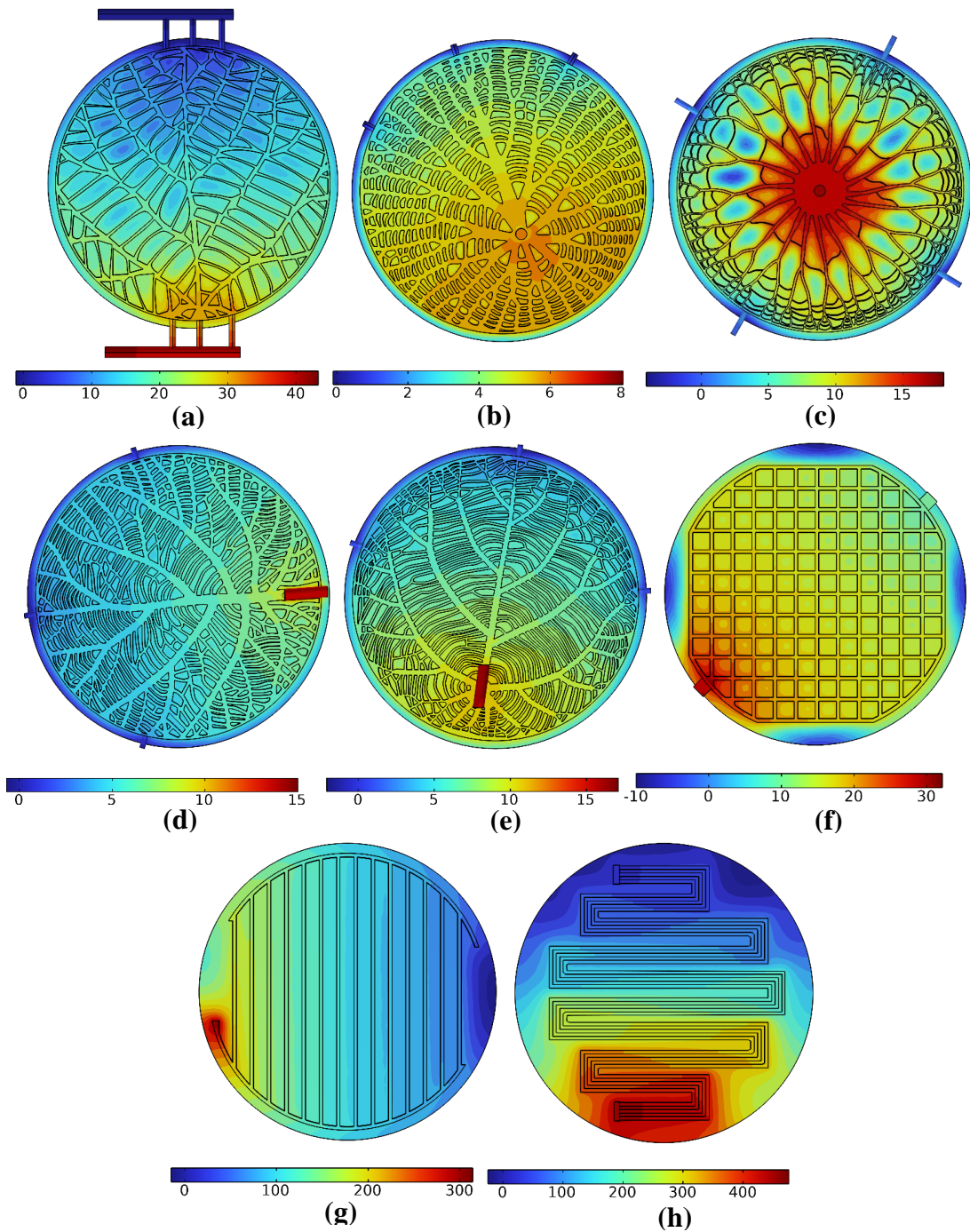
Figure 3.5 Pressure distribution for all the models with pressure Pa scales vary depending on the design itself; (a) L1U Soybeans, (b) L2V Victoria Amazonica Water Lily, (c) L3N nelumbo nucifera, (d) L4K Kiwi, (e) L5A Acalypha Hispida, (f) PO7 point, (g) PR6 Parallel, (h) SR8 Serpentine.

As depicted in Figure 3.4 (b). The leaf bio-inspired models, particularly L2V with an 8.05 Pa pressure drop, showcase substantially lower pressure drops in the range of 0 to 45 Pa, as opposed to traditional models. Pressure distribution indicates higher values at channel entrances, diminishing along the channel due to friction and local flow redirection. Figure 3.5. demonstrates static pressure across various flow field designs, with varied pressure scales contingent upon design nuances. The spiral path within channels notably contributes to pressure drop, as indicated in Figure 3.5 (h). The increased number of connections in leaf bio-inspired models, notably L2V, L4K, and L5A, ensures quicker pressure equalization, resulting in more uniform pressure distribution and lower pressure drop contours. These models exhibit highly interconnected flow channels, enhancing homogeneity and minimizing pressure differentials, as indicated in Figure 3.5 (b), (d), (e).

3.3 Mixture Distribution

The distribution of reactant mass fractions ideally aligns with the velocity profile, aiming for higher reactant mass fractions to enhance reaction rates, consequently ensuring more uniform reactant density and consistent current density across the cell. Figure 3.6 (a - c). illustrates the distribution of oxygen concentration within the anode compartment and the anode GDL at a specific current density of 15000 A/m^2 . The findings reveal an increment in oxygen concentration along the channel owing to increased pressure drop and water consumption. At the inlet of the channel, higher water availability leads to lower reactant diffusion rates, causing a gradual decrease in water concentration as the mixture progresses toward the outlet. Consequently, oxygen concentration remains closer to zero at the inlet. Besides that, a Ti mesh is used as material for the anode GDL which makes it able to reach this amount of mixture concentration as shown in Figure 3.6 (a - c).

Figure 3.7. displays water distribution among various flow field designs, maintaining identical Water Mole Fraction distribution scales for all designs. A comparison between traditional and leaf bio-inspired models indicates a notably more

uniformly homogeneous water distribution in leaf bio-inspired models. By analyzing Figure 3.8. particularly evident in the L2V, L4K, and L5A designs in contrast to point,
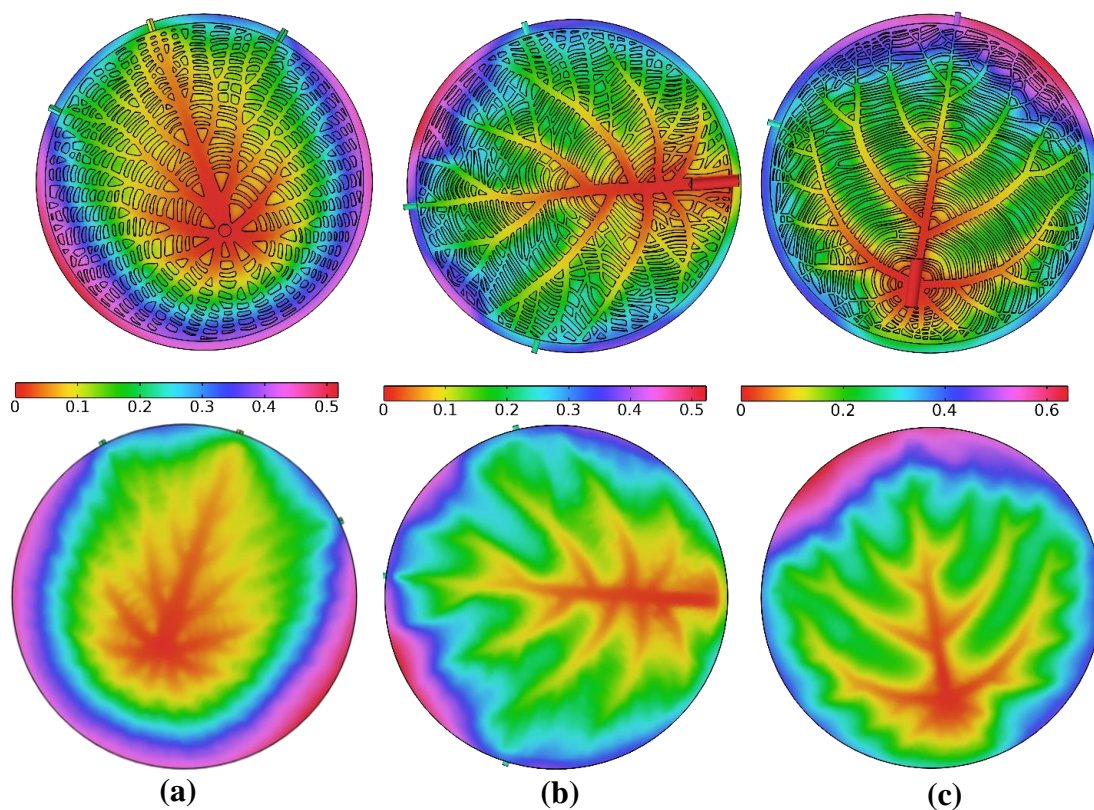
Figure 3.6 Oxygen Mole Fraction distribution for leaf bio-inspired models within the anode compartment and the anode GDL with Mole Fraction (1) scales vary depending on the design itself, and at the GDL of the models ; (a) L2V Victoria Amazonica Water Lily, (b) L2V Victoria Amazonica Water Lily, (b) L4K Kiwi, (c) L5A Acalypha Hispida.

parallel, and multi-serpentine models, respectively. The achievement of more high-performance cells correlates with the adoption of designs fostering a uniformly homogeneous distribution pattern.
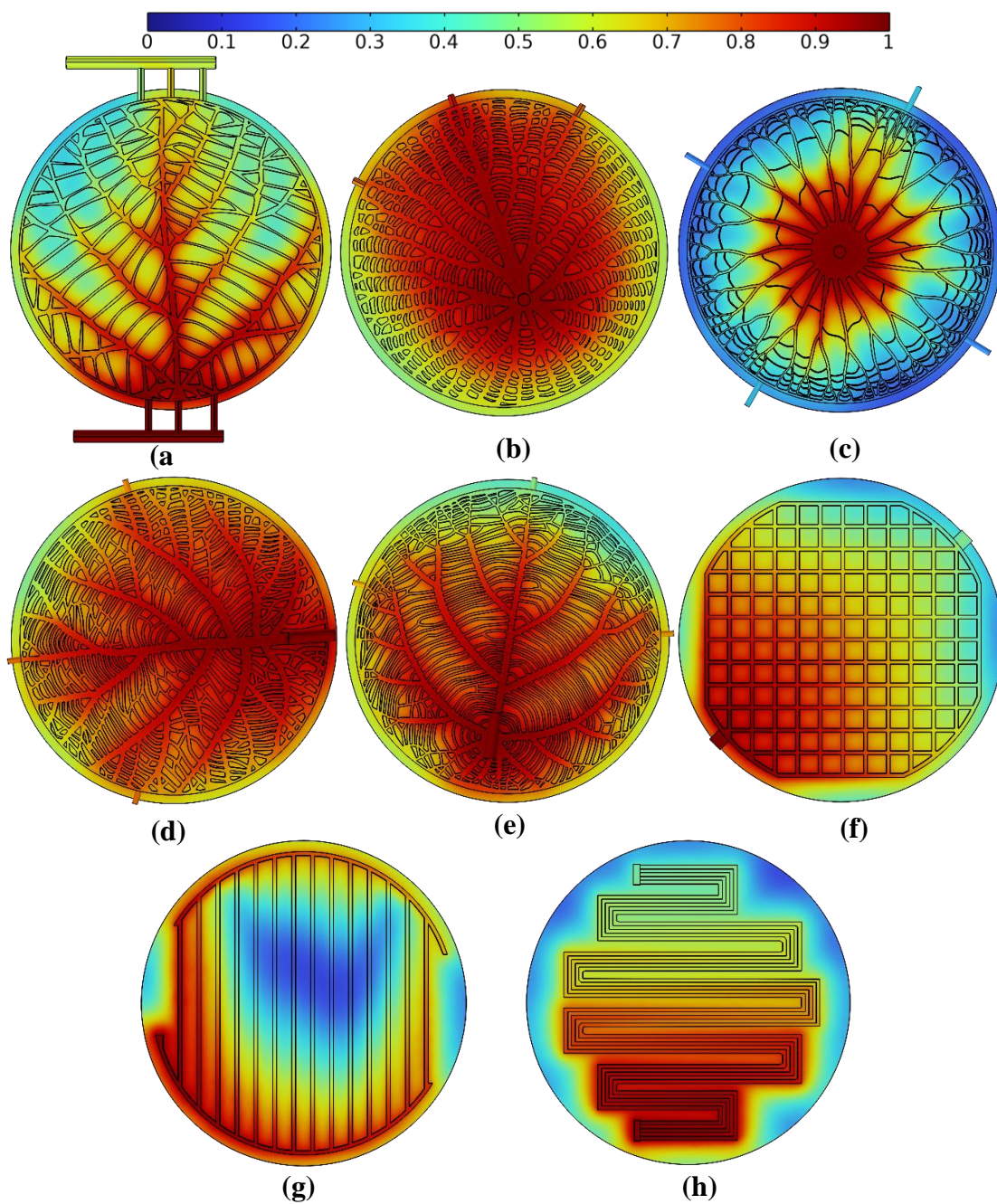
Figure 3.7 Water Mole Fraction distribution for all the models with one Mole Fraction scale from 0 to 1 (1) ; (a) L1U Soybeans, (b) L2V Victoria Amazonica Water Lily, (c) L3N nelumbo nucifera, (d) L4K Kiwi, (e) L5A Acalypha Hispida, (f) PO7 point, (g) PR6 Parallel, (h) SR8 Serpentine.

Figure 3.8 Water Mole Fraction distribution for all the models with Mole Fraction (1) scales vary depending on the design itself ; (a) L1U Soybeans, (b) L2V Victoria Amazonica Water Lily, (c) L3N nelumbo nucifera, (d) L4K Kiwi, (e) L5A Acalypha Hispida, (f) PO7 point, (g) PR6 Parallel, (h) SR8 Serpentine.

3.4   Velocity Distribution

PEMWE systems derive substantial benefits from uniform and high-velocity profiles. Elevated velocities significantly improve a cell's ability to expel liquid water and expedite the extraction of generated gases, thereby enhancing operational efficiency.

Similar reactant residence times and more even reactant distribution characterize uniform velocity profiles, resulting in a more consistent distribution of hydrogen production. Consequently, Figure 3.9. depicts the velocity magnitude contours of various flow field designs within the anode channel at a specific current density of 15000 A/m^2 , utilizing a single specified velocity scale. Leaf bio-inspired models showcase lower maximum velocities while demonstrating swifter water removal at higher maximum velocities. Notably, in traditional models, maximum velocities primarily occur at channel inlets, after which average velocities drop below those of leaf bio-inspired models. Consequently, the L2V, L4K, and L5A models exhibit higher average velocities compared to traditional models. Moreover, leaf models achieve almost uniform and stable average velocities in contrast to traditional designs, which exhibit high inlet and low channel velocities. Uniform velocity profiles contribute to a more even distribution of reactants, as depicted in Figure 3.10. However, it's important to note that velocity scales vary based on the design. Notably, the leaf bio-inspired model demonstrates a remarkably homogeneous velocity distribution with a narrow range of high-magnitude velocities along the channel. In terms of velocity profiles, the L2V, L4K, and L5A models notably outperform other designs. And as shown in the Figure 3.11. the velocity factor and the stream line evident that the L2V has the best velocity profile.
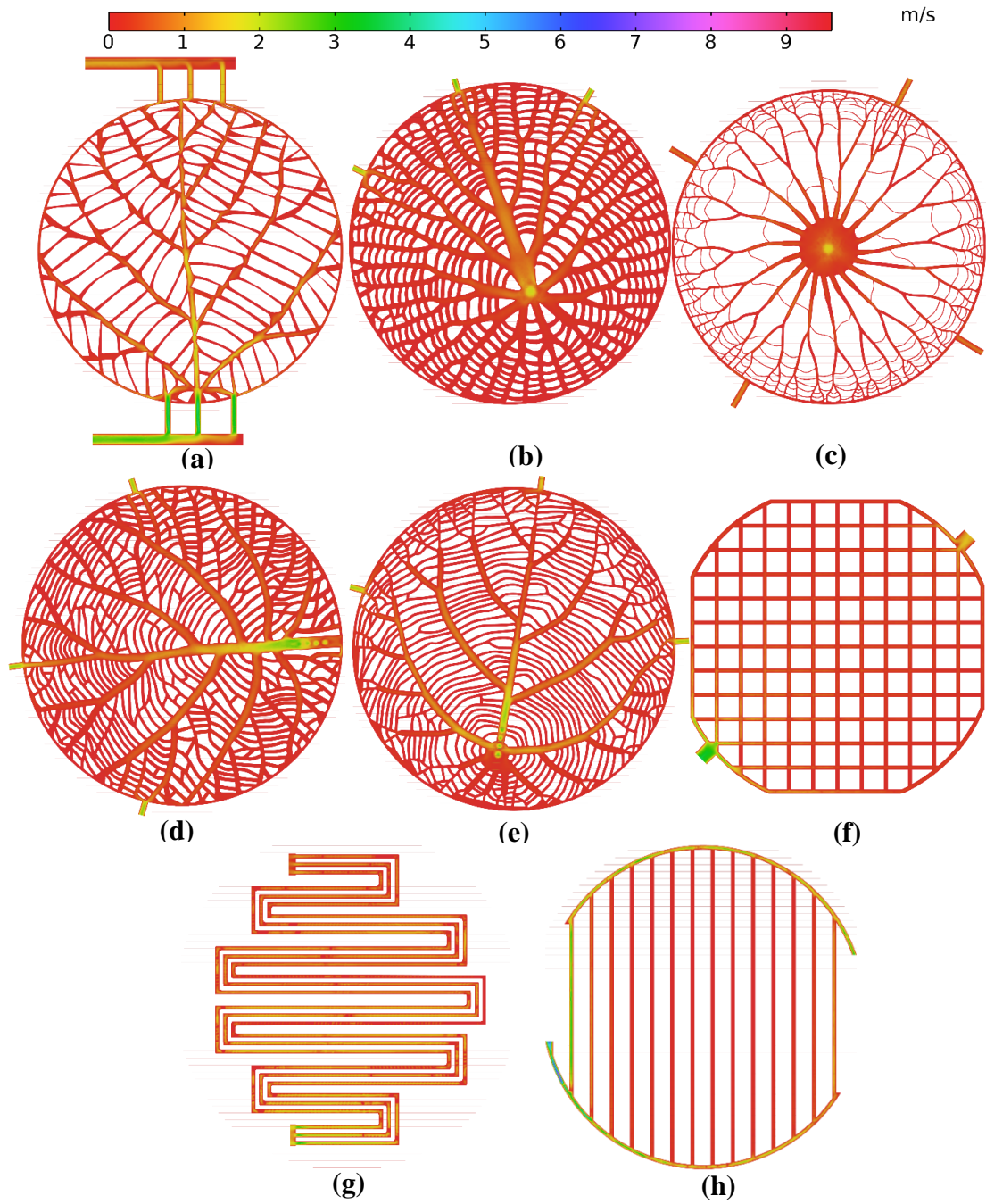
Figure 3.9 Water Channels Velocity distribution for all the models with one Velocity scale from 0 to 9.6 m/s ; (a) L1U Soybeans, (b) L2V Victoria Amazonica Water Lily, (c) L3N nelumbo nucifera, (d) L4K Kiwi, (e) L5A Acalypha Hispida, (f) PO7 point, (g) PR6 Parallel, (h) SR8 Serpentine.
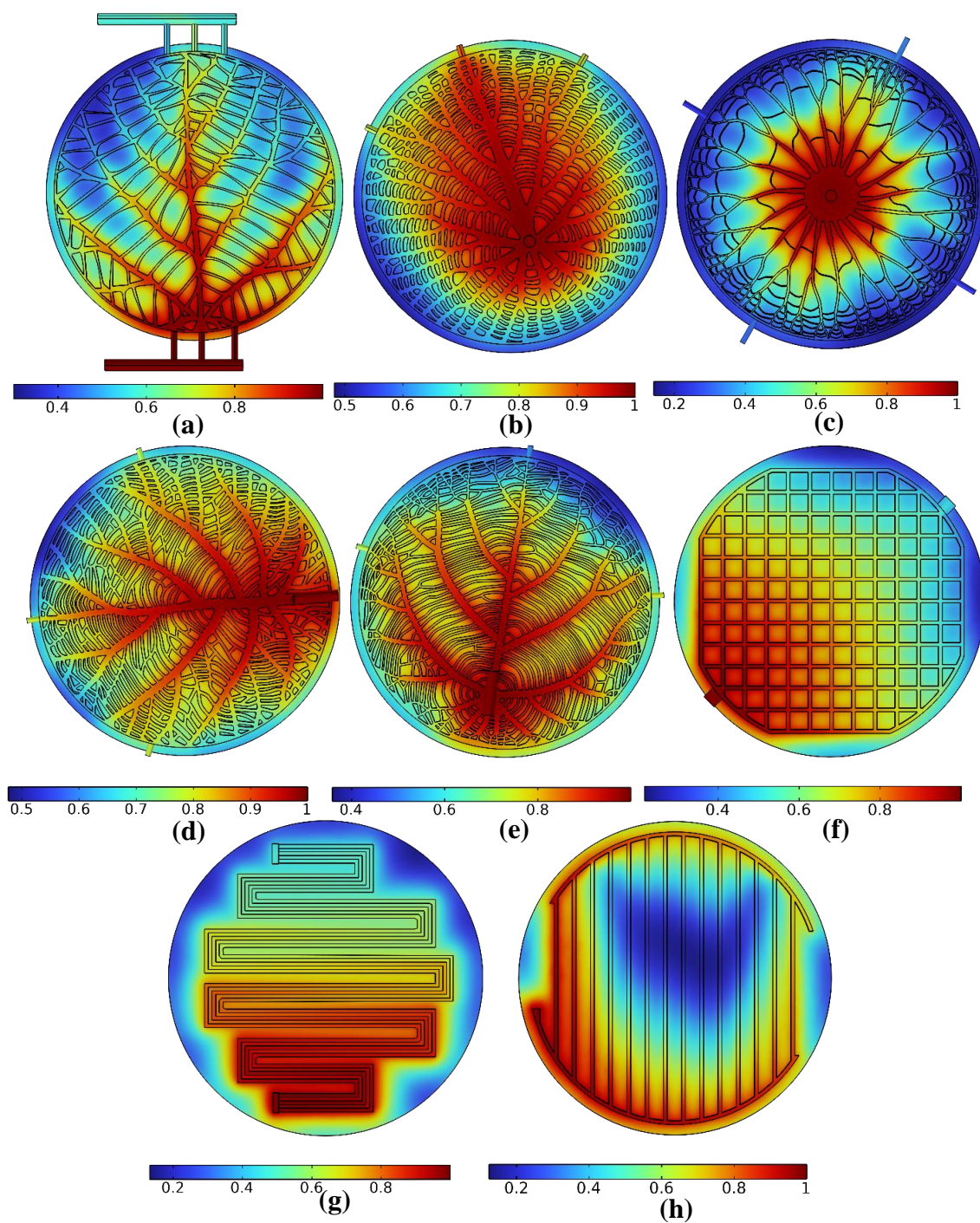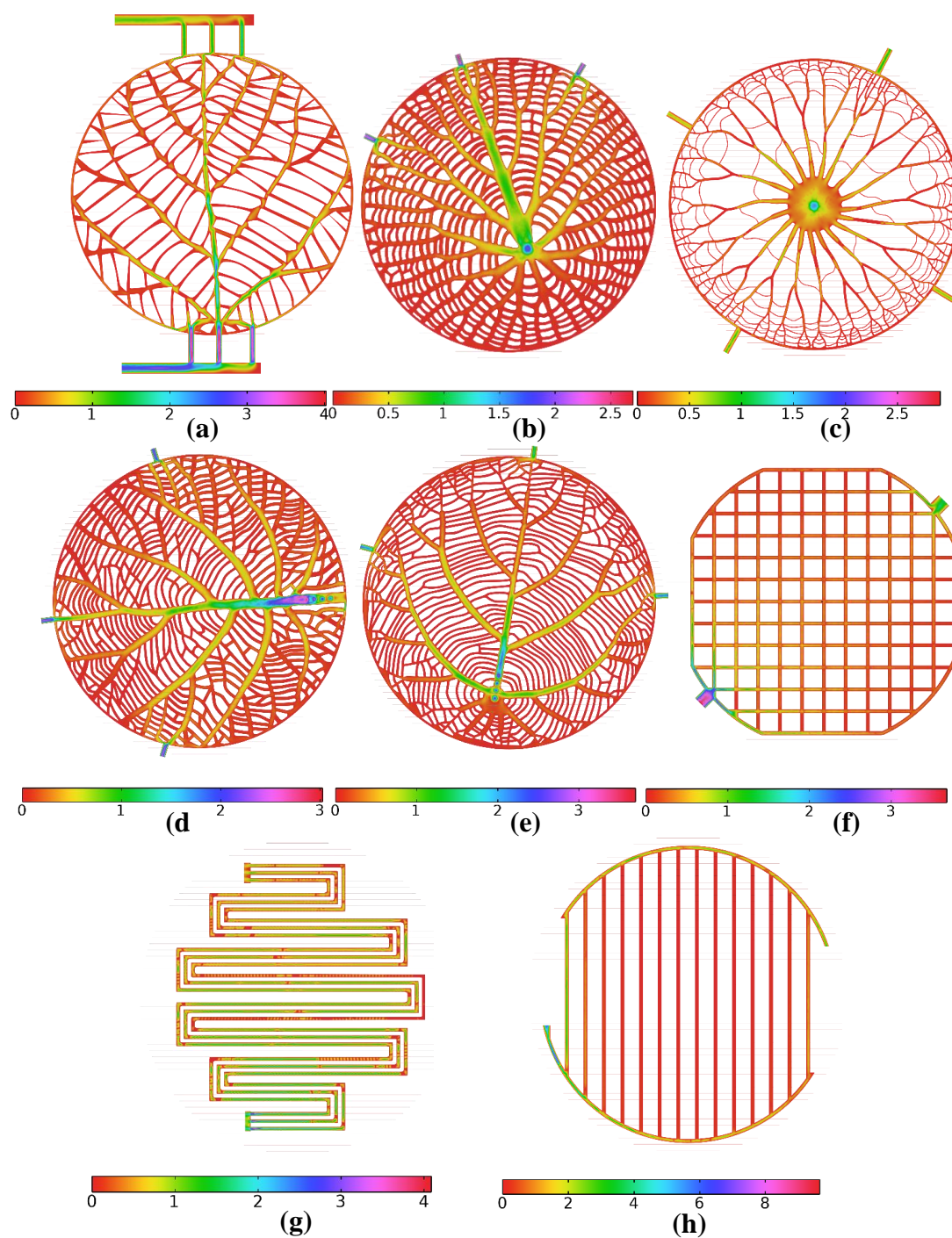
Figure 3.10 Water Channels Velocity distribution for all the models with Velocity m/s scales vary depending on the design itself ; (a) L1U Soybeans, (b) L2V Victoria Amazonica Water Lily, (c) L3N nelumbo nucifera, (d) L4K Kiwi, (e) L5A Acalypha Hispida, (f) PO7 point, (g) PR6 Parallel, (h) SR8 Serpentine.
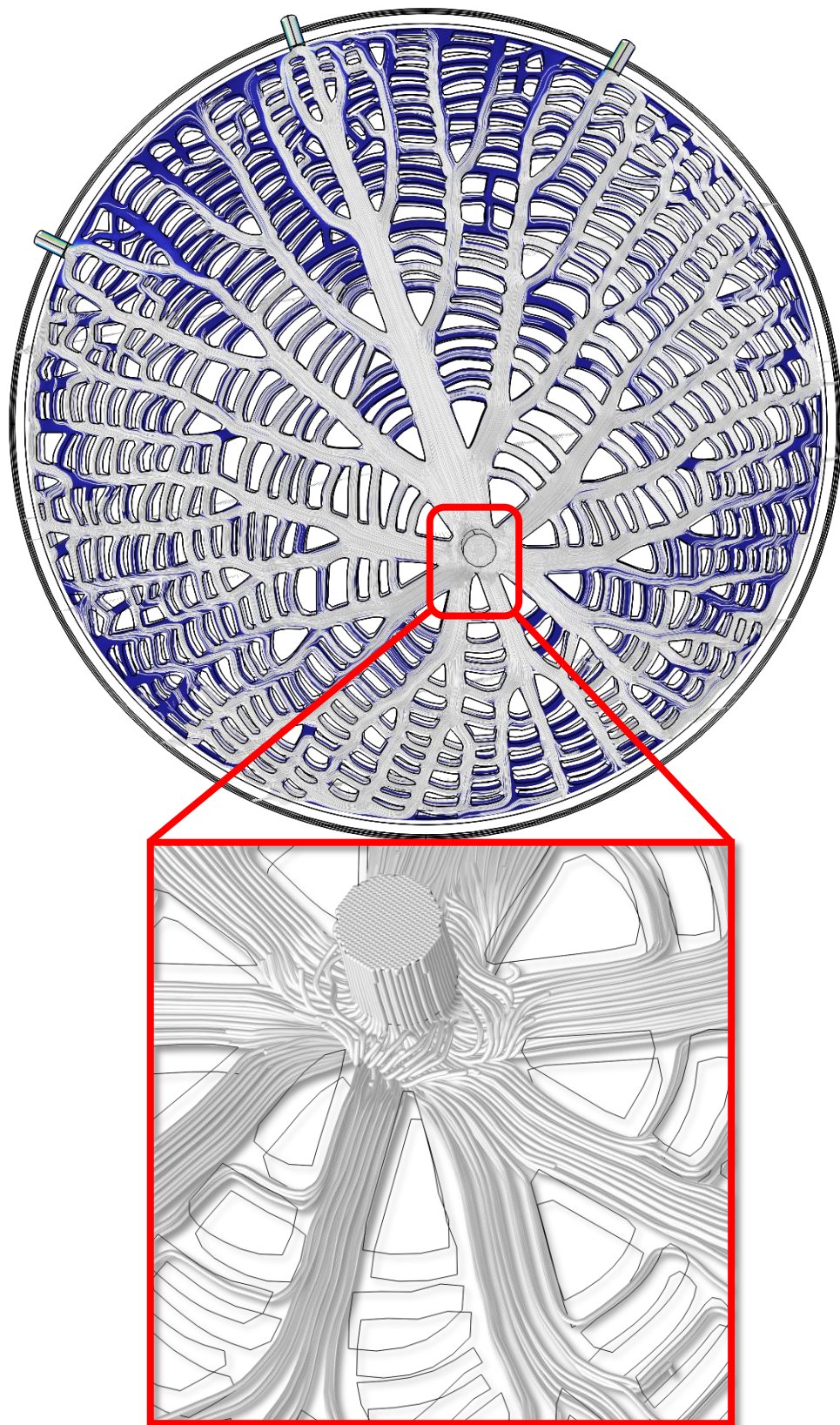
Figure 3.11 Mixture Channels Velocity streamline (velocity vector) m/s for L2V Victoria Amazonica Water Lily.

3.5   Optimization Study

In aim to utilize and optimize the PEMWE leaf bio-inspired models, some analysis has been done to study the effects of mass flow rate, exchange current density, active specific surface area (ASSA), and operation temperature on the voltage, pressure drop, and velocities.

3.5.1   Mass Flow Rate Affects

As a result, Figure 3.11. explains how mass flow rate affects the pressure drop and average velocity of the L2V, L4K, and L5A models at a specific current density of 15000 A/m^2 , 328.15 K temperature, and a pressure of 1 bar with variable mass flow rate controlled by equation (28). The velocity increases as the mass flow rate increases resulting in a higher performance while pressure increases linearly with the mass flow rate in turn to worse performance, which on the other hand count no effect on the voltage.
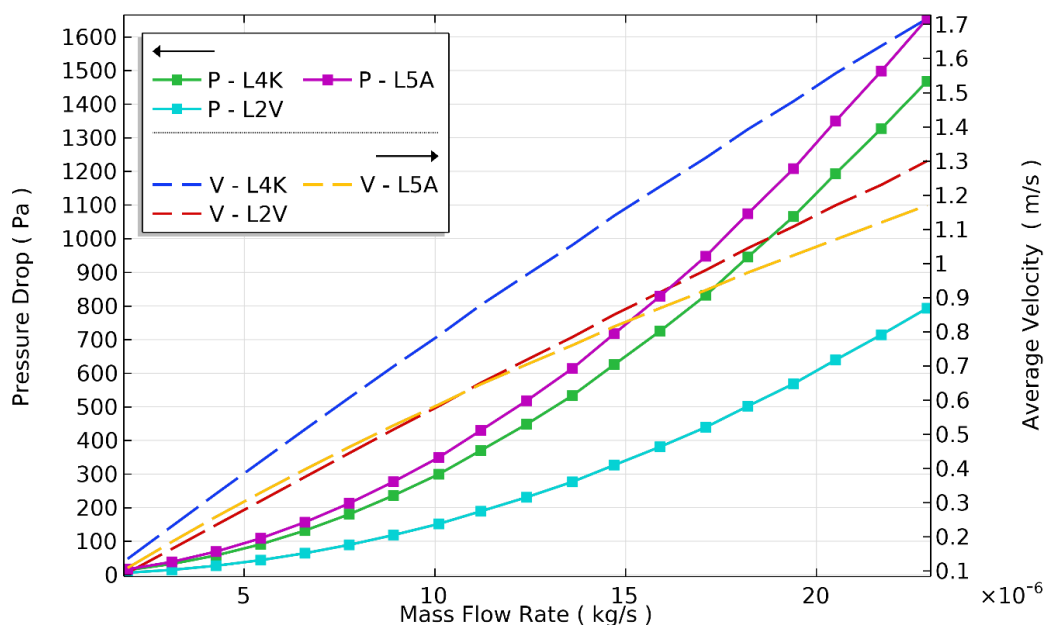
Figure 3.12 Effects of mass flow rate kg/s on the pressure drop Pa (P- model name) and average velocity m/s (V- model name) of; L2V Victoria Amazonica Water Lily, L4K Kiwi, and L5A Acalypha Hispida.

3.5.2 Reference Exchange Current Density

The effect of the anode-cathode Reference exchange current density on Polarization curves is illustrated in Figure 3.12. Using [58] study's anode-cathode Reference exchange current density values compared to this study's values while keeping the operation condition the same. Shows that increasing the anode-cathode Reference exchange current density led to better Polarization curve performance while recording no effect on the pressure drop and velocity.
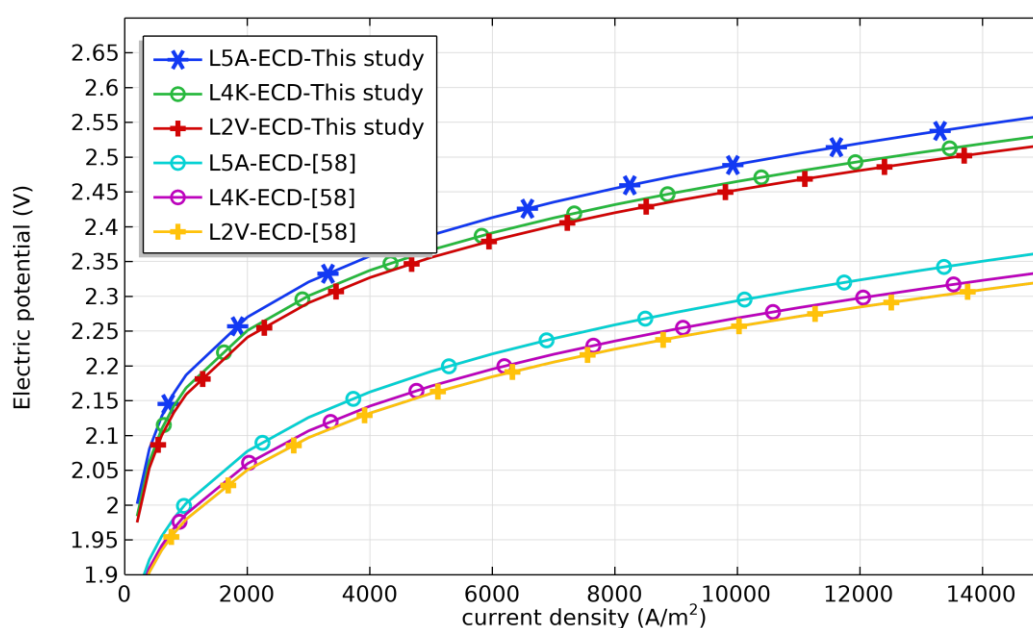
Figure 3.13 Effects of Reference Exchange Current Density A/m^2 (ECD) on the Polarization curves of; L2V Victoria Amazonica Water Lily, L4K Kiwi, and L5A Acalypha Hispida.

3.5.3 Active Specific Surface Area (ASSA)

Figure 3.13 Shows how the Active specific surface area $1/m$ related to the anode and cathode catalyst has a significant effect on the Polarization curves using five different values within a 1E4 to 1E8, so by increasing the ASSA voltage decreases, which in turn improves Polarization curve performance in a sufficient way, while having no considerable effect on the pressure drop, O_2 Mole fraction, and average velocity as depicted in Figure 3.14 With 5.43 mg/s mass flow rate.
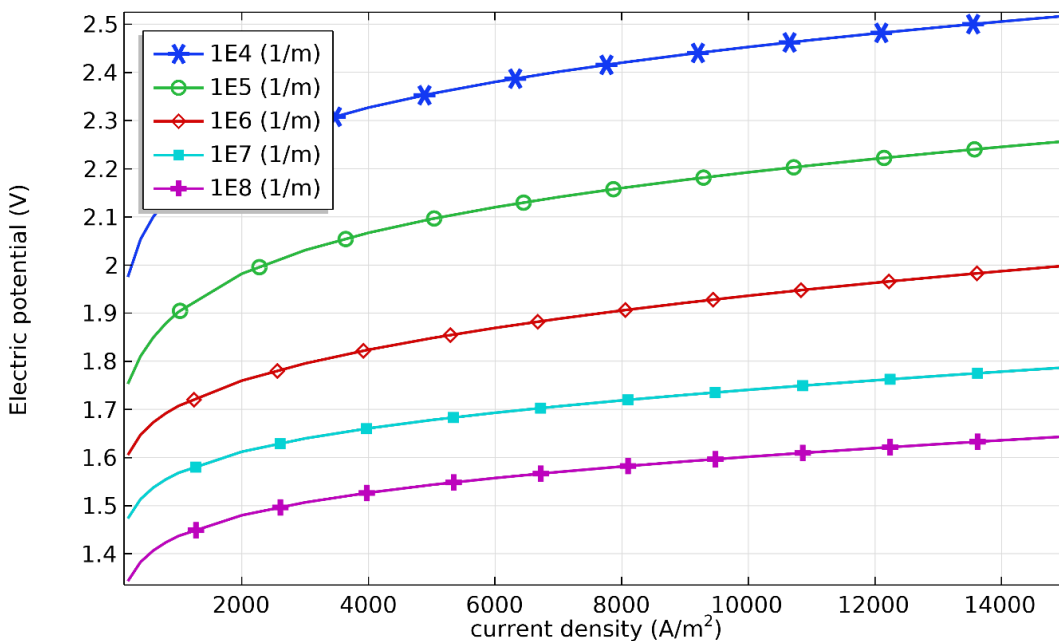
Figure 3.15 Effects of Active specific surface area 1/m on the Polarization curves of; L2V Victoria Amazonica Water Lily for five ASSA values form 1E4 to 1E8.

Figure 3.14 Effects of Active specific surface area 1/m on the pressure drop Pa, O_2 Mole fraction (1), and average velocity m/s of; L2V Victoria Amazonica Water Lily for five ASSA values form 1E4 to 1E8 1/m.

3.5.4 Operation Temperature

As well operation temperature is an important factor affecting the PEMWE so in Figure 3.15. Illustrates the Polarization curves of the L2V model at four different operation temperature values from 308.15 to 368.18 K , finding that working on lower operation temperature gives a higher polarization curve performance. Figure 3.16. explain how the operation temperature has almost no effect on the O_2 Mole fraction, and average velocity at 1.94 mg/s mass flow rate , while as temperature increases the pressure drop slightly increases.

Figure 3.16 Effects of Operation Temperature K on the Polarization curves of; L2V Victoria Amazonica Water Lily for four operation temperature values from 308.15 to 368.18 K.
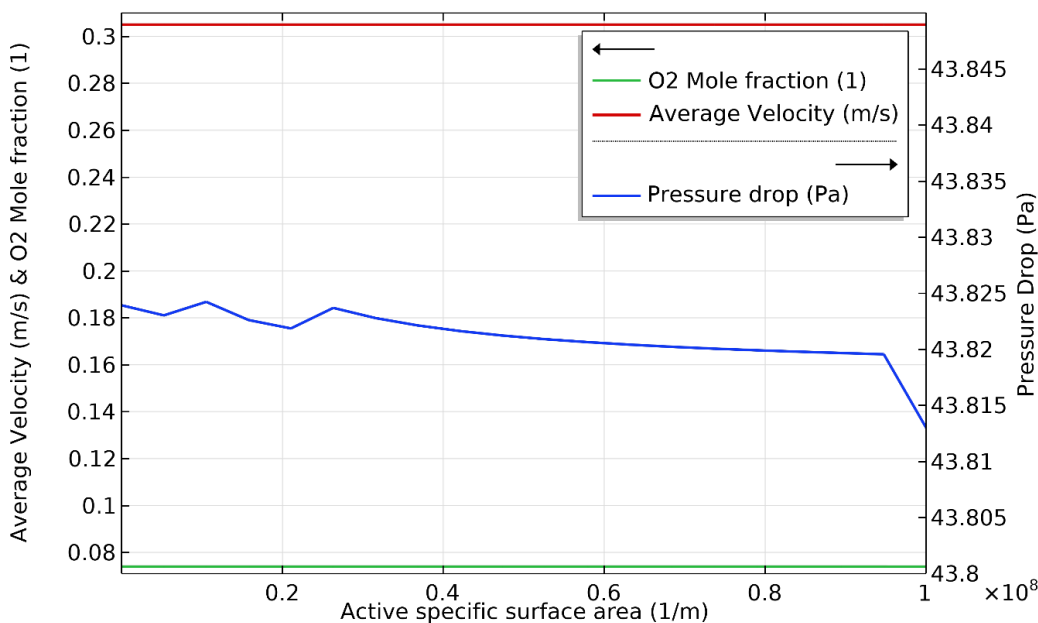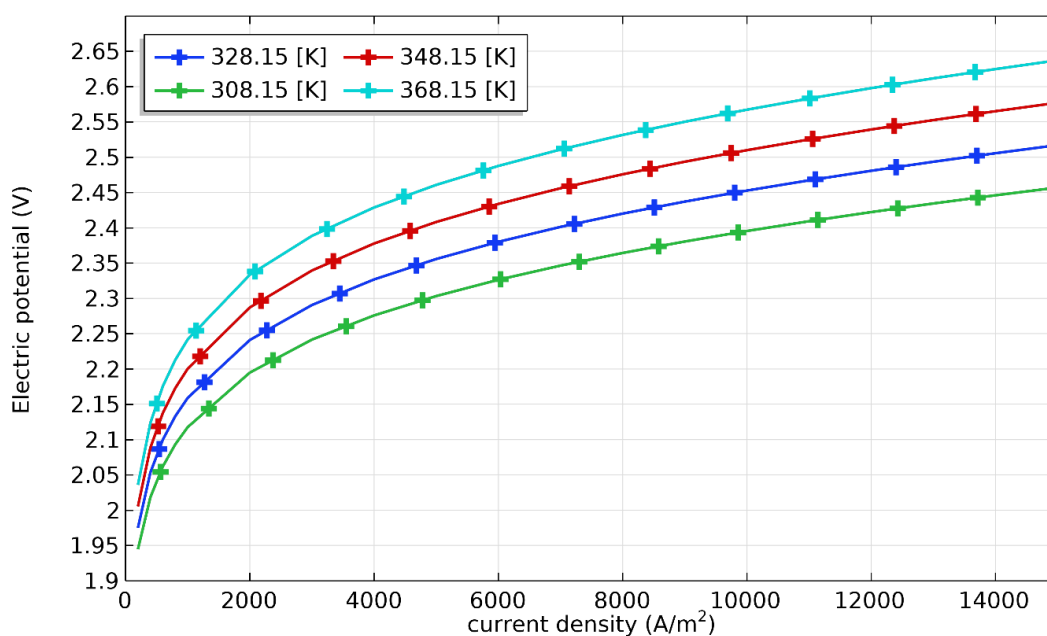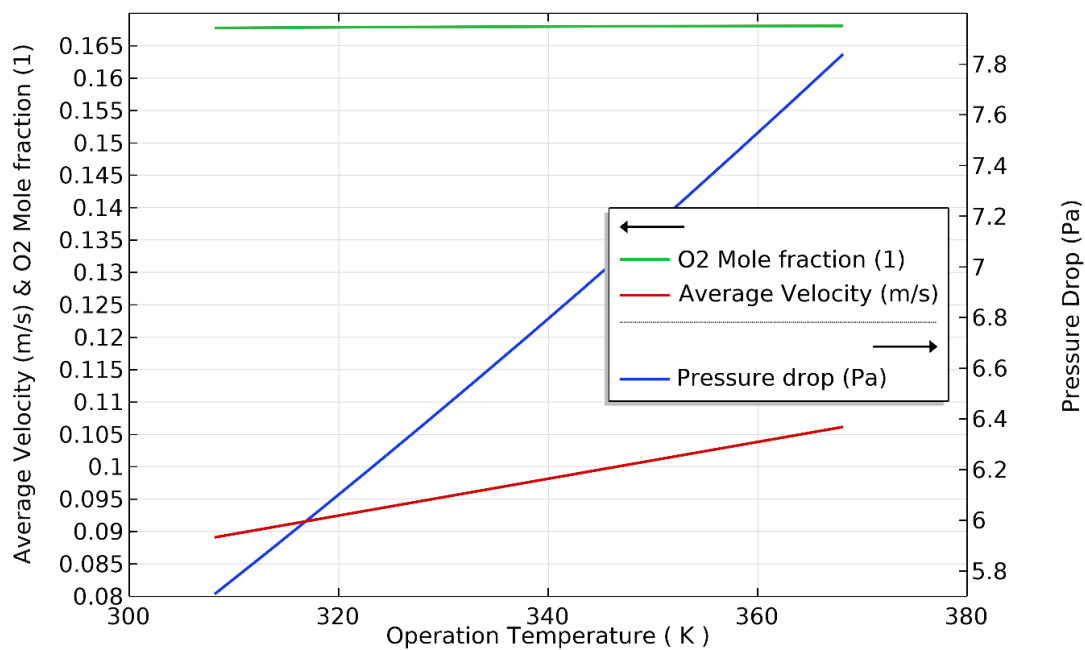
Figure 3.17 Effects of Operation Temperature K on the pressure drop Pa, O_2 Mole fraction

(1), and average velocity m/s of; L2V Victoria Amazonica Water Lily four values from

308.15 to 368.18 K.

CHAPTER 4

CONCLUSION

Electrolysis paired with renewable energy sources emerges as a highly auspicious method for green hydrogen production. Within the spectrum of electrolysis approaches, the Polymer Electrolyte Membrane Water Electrolyzer (PEMWE) is the most chosen and preferred return on its capacity for producing compressed, high-purity hydrogen. The design of bipolar plates and their channel patterns notably influence the performance and durability of the PEM water electrolyzer. In this study, a Three-dimensional, numerical, steady state, multi-component, single phase model, utilizing COMSOL Multiphysics Software of exact leaf bio-inspired geometry is employed as a novel bipolar plate channel pattern. A Parallel, point, and Serpentine model as a traditional model with five different leaf bio-inspired models brought in comparison to analyze the benefits of this innovative design and the improvements it achieves to the bipolar plate and in turn to the PEMWE. At 328.15 K operating temperature, 1 bar pressure, and variable mass flow rate on 200 to 15000 A/m^2 current density range.

The model result shows that leaf bio-inspired models show lower polarization curves compared to the traditional model ones with the best polarization curve performance for the L2V, L4K, and L5A models respectively. In L2V at 15000 A/m^2 current density, the voltage is lower than parallel, serpentine, and point flow channels up to 5%, 4.1%, and 4% respectively. Regarding pressure, particularly L2V with an 8.05 Pa pressure drop exhibits the lowest pressure drop among all models, at 15000 A/m^2 current density, the pressure drop is lower than parallel, serpentine, and point flow channels up to 97.9%, 98.6 %, and 79.3% respectively. Besides that, L2V, L4K, and L5A models have the best homogeneous uniform distribution. Evident in the L2V, L4K, and L5A designs in contrast to point, parallel, and multi-serpentine models, a uniformly homogeneous water distribution in leaf bio-inspired models is indicated including Ti mesh, so at 15000 A/m^2 current density, the L2V is more homogeneous

than parallel, serpentine, and point flow channels by 40.8%, 40.1 %, and 33.6% respectively. The L2V, L4K, and L5A models exhibit more appropriate higher average velocities compared to traditional models. Moreover, leaf bio-inspired models achieve almost uniform and stable average velocity distribution with a narrow range of high-magnitude velocities along the channel, which gives the leaf models a high homogeneity and mixture removability. Achieving the best polarization curve performance, lower pressure drop, and the most uniformly homogeneous pressure and velocity distributions, makes the leaf bio-inspired bipolar plate designs the optimum highest performance designs over other conventional designs.

It's been found from the optimization study that increasing the mass flow rate led to a high increment in the pressure and average velocity, while active specific surface area and operation temperature have no countable effect on O_2 Mole fraction and average velocity. On the other hand, the active specific surface area, operation temperature, and reference exchange current density have a major effect on the polarization curves on leaf bio-inspired PEMWE models. that increasing the anode-cathode Reference exchange current density and active specific surface area and lowering the operation temperature gives an optimum high PEMWE polarization curve performance.

4.1 Recommendation and Future Work

Further questions arising from the simulation of an innovative flow-field architecture based on a bio-inspired pattern for PEM water electrolysis can delve into a variety of topics to improve understanding and expand the practical applications of the technology in the fields of green energy and green hydrogen. Optimizing the parameters of the bio-inspired pattern to maximize output and efficiency could be one direction for future research. For practical application, it is essential to investigate the flow-field design's long-term stability and durability, taking into account factors like the shapes of the channel cross-section, which can be circular or triangular, under a variety of operating conditions. In addition, life cycle and economic analyses could be

performed to evaluate the general viability and sustainability of putting such creative designs into practice on a broader scale. Cost-effective studies are essential given the high initial costs of fabrication and manufacturing associated with this design. These directions for future research have the potential to greatly advance the field, solve problems, and improve the bio-inspired flow-field design for PEM water electrolysis in the context of hydrogen production and green energy.

REFERENCES

[1]   Ashraf, S., Raja Sekar, T., & Abraham, J. Relationships among environmental pollution, energy use and economic growth: a global perspective. OPEC Energy Review, *(4)*, (44) 511-534. 2020

[2]   Laldjebaev, M., Isaev, R., & Saukhimov, A. Renewable energy in Central Asia: An overview of potentials, deployment, outlook, and barriers. Energy Reports, *(7)*, 3125-3136. 2021

[3]   Smolinka, T., Ojong, E. T., & Garche, J. hydrogen production from renewable energies electrolyzer technologies. Elsevier - In Electrochemical energy storage for renewable sources and grid balancing 103-128. 2015

[4]   Nagasawa, K., Kato, A., Nishiki, Y., Matsumura, Y., Atobe, M., & Mitsushima, S. The effect of flow-field structure in toluene hydrogenation electrolyzer for energy carrier synthesis system. Electrochimica Acta, *(246)*, 459-465. 2017

[5]   Hosseini, S. E., & Wahid, M. A. Hydrogen production from renewable and sustainable energy resources: Promising green energy carrier for clean development. Renewable and Sustainable Energy Reviews, *(57)*, 850-866. 2016

[6]   Depcik, C., Cassady, T., Collicott, B., Burugupally, S. P., Li, X., Alam, S. S., & Hobeck, J. Comparison of lithium ion Batteries, hydrogen fueled combustion Engines, and a hydrogen fuel cell in powering a small Unmanned Aerial Vehicle. Energy conversion and management, *(207)*, 112514. 2020

[7]   IEA   (2023), Global   Hydrogen   Review   2023,   IEA,   Paris https://www.iea.org/reports/global-hydrogen-review-2023, License: CC BY 4.0

[8]   IEA   (2019), The   Future   of   Hydrogen,   IEA,   Paris https://www.iea.org/reports/the-future-of-hydrogen, License: CC BY 4.0

[9]   Akhlaghi, N., & Najafpour-Darzi, G. A comprehensive review on biological hydrogen production. International Journal of Hydrogen Energy, *(43)*, (45) 22492-22512. 2020

[10]   Anwar, S., Khan, F., Zhang, Y., & Djire, A. Recent development in electrocatalysts for hydrogen production through water electrolysis. International Journal of Hydrogen Energy, *(63)*, (46) 32284-32317. 2021

[11]   Brauns, J., & Turek, T. Alkaline water electrolysis powered by renewable energy. Processes, *(2)*, (8) 248. 2020

[12]   Miller, H. A., Bouzek, K., Hnat, J., Loos, S., Bernäcker, C. I., Weißgärber, T., & Meier-Haack, J. Green hydrogen from anion exchange membrane water electrolysis: a review of recent developments in critical materials and operating conditions. Sustainable Energy & Fuels, *(5)*, (4) 2114-2133. 2020

[13]   Sebbahi, S., Nabil, N., Alaoui-Belghiti, A., Laasri, S., Rachidi, S., & Hajjaji, A. Assessment of the three most developed water electrolysis technologies: Alkaline water electrolysis, proton exchange membrane and solid-oxide electrolysis. Materials Today: Proceedings, *(66)*, 140-145. 2022

[14]   Bazarah, A., Majlan, E. H., Husaini, T., Zainoodin, A. M., Alshami, I, Goh, J., & Masdar, M. S. Factors influencing the performance and durability of polymer electrolyte membrane water electrolyzer: A review. International Journal of Hydrogen Energy, *(85)*, (47) 35976-35989. 2022

[15]   Kuhnert, Eveline, Viktor Hacker, & Merit Bodner. "A Review of Accelerated Stress Tests for Enhancing MEA Durability in PEM Water Electrolysis Cells." International journal of energy research 2023 (2023).

[16]   Shirvanian, P., & van Berkel, F. Novel components in Proton Exchange Membrane (PEM) Water Electrolyzers (PEMWE): Status, challenges and

future needs. A mini review. Electrochemistry Communications, *(114)*, 106704. 2020

[17]   Teuku, H., Alshami, I., Goh, J., Masdar, M. S., & Loh, K. S. Review on bipolar plates for low-temperature polymer electrolyte membrane water electrolyzer. International Journal of Energy Research, *(15)*, (45) 20583-20600. 2021

[18]   Ahmed, K. W., Jang, M. J., Park, M. G., Chen, Z., & Fowler, M. Effect of components and operating conditions on the performance of PEM electrolyzers: a review. Electrochem, *(4)*, (3) 581-612. 2022

[19]   Li, W., Zhang, Q., Wang, C., Yan, X., Shen, S., Xia, G., & Zhang, J. Experimental and numerical analysis of a three-dimensional flow field for PEMFCs. Applied Energy, *(195)*, 278-288. 2017

[20]   Heidary, H., Kermani, M. J., Prasad, A. K., Advani, S. G., & Dabir, B. Numerical modelling of in line and staggered blockages in parallel flowfield channels of PEM fuel cells. International journal of hydrogen energy, *(4)*, (42), 2265-2277. 2017

[21]   Lim, B. H., Majlan, E. H., Daud, W. R. W., Rosli, M. I., & Husaini, T. Numerical analysis of modified parallel flow field designs for fuel cells. International Journal of Hydrogen Energy, *(14)*, (42), 9210-9218. 2017

[22]   Wang, Y., Wang, S., Wang, G., & Yue, L. Numerical study of a new cathode flow-field design with a sub-channel for a parallel flow-field polymer electrolyte membrane fuel cell. International Journal of Hydrogen Energy, *(43)*, (4), 2359-2368. 2018

[23]   Liu, H., Yang, W., Tan, J., An, Y., & Cheng, L. Numerical analysis of parallel flow fields improved by micro distributor in proton exchange membrane fuel cells. Energy Conversion and Management, *(176)*, 99-109. 2018

[24]   Penga, Ž., Bergbreiter, C., Barbir, F., & Scholta, J. Numerical and experimental analysis of liquid water distribution in PEM fuel cells. Energy Conversion and Management, *(189)*, 167-183. 2019

[25]   Atyabi, S. A., & Afshari, E. A numerical multiphase CFD simulation for PEMFC with parallel sinusoidal flow fields. Journal of Thermal Analysis and Calorimetry, *(135)*, 1823-1833. 2019

[26]   Wang, Y., Du, Y., Ni, M., Zhan, R., Du, Q., & Jiao, K. Three-dimensional modeling of flow field optimization for co-electrolysis solid oxide electrolysis cell. Applied Thermal Engineering, *(172)*, 114959. 2020

[27]   Limjeerajarus, N., & Santiprasertkul, T. Novel hybrid serpentine-interdigitated flow field with multi-inlets and outlets of gas flow channels for PEFC applications. International Journal of Hydrogen Energy, *(25)*, (45) 13601-13611. 2020

[28]   Rahimi-Esbo, M., Ranjbar, A. A., Ramiar, A., Alizadeh, E., & Aghaee, M. Improving PEM fuel cell performance and effective water removal by using a novel gas flow field. international journal of hydrogen energy, *(4)*, (41) 3023-3037. 2016

[29]   Kim, A. R., Shin, S., & Um, S. Multidisciplinary approaches to metallic bipolar plate design with bypass flow fields through deformable gas diffusion media of polymer electrolyte fuel cells. Energy, *(106)*, 378-389. 2016

[30]   Alizadeh, E., Rahimi-Esbo, M., Rahgoshay, S. M., Saadat, S. H. M., & Khorshidian, M. Numerical and experimental investigation of cascade type

serpentine flow field of reactant gases for improving performance of PEM fuel cell. International Journal of Hydrogen Energy, *(21)*, (42) 14708-14724. 2017

[31]   Liu, H. C., Yang, W. M., Cheng, L. S., & Tan, J. Numerical Analysis of Different Multi-serpentine Flow Fields for Proton Exchange Membrane Fuel Cells. Fuel Cells, *(18)*, (2) 173-180. 2018

[32]   Vijayakrishnan, M. K., Palaniswamy, K., Ramasamy, J., Kumaresan, T., Manoharan, K., Rajagopal, T. K. R., & Yi, S. C. Numerical and experimental investigation on 25 cm^2 and 100 cm^2 PEMFC with novel sinuous flow field for effective water removal and enhanced performance. International Journal of Hydrogen Energy, *(13)*, (45) 7848-7862. 2020

[33]   Chowdhury, M. Z., & Akansu, Y. E. Novel convergent-divergent serpentine flow fields effect on PEM fuel cell performance. International Journal of Hydrogen Energy, *(40)*, (42) 25686-25694. 2017

[34]   Havaej, P. A numerical investigation of the performance of Polymer Electrolyte Membrane fuel cell with the converging-diverging flow field using two-phase flow modeling. Energy, *(182)*, 656-672. 2019

[35]   Wang, B., Chen, W., Pan, F., Wu, S., Zhang, G., Park, J. W., & Jiao, K. A dot matrix and sloping baffle cathode flow field of proton exchange membrane fuel cell. Journal of Power Sources, *(434)*, 226741. 2019

[36]   Zhang, G., Xie, B., Bao, Z., Niu, Z., & Jiao, K. Multi-phase simulation of proton exchange membrane fuel cell with 3D fine mesh flow field. International Journal of Energy Research, *(15)*, (42) 4697-4709. 2018

[37]   Nie, J., & Chen, Y. Numerical modeling of three-dimensional two-phase gas iquid flow in the flow field plate of a PEM electrolysis cell. International Journal of Hydrogen Energy, *(8)*, (35) 3183-3197. 2010

[38] Olesen, A. C., Rømer, C., & Kær, S. K. A numerical study of the gas liquid, two phase flow maldistribution in the anode of a high pressure PEM water electrolysis cell. International Journal of Hydrogen Energy, *(1)*, (41) 52-68. 2016

[39] Toghyani, S., Afshari, E., & Baniasadi, E. Three-dimensional computational fluid dynamics modeling of proton exchange membrane electrolyzer with new flow field pattern. Journal of Thermal Analysis and Calorimetry, *(135)*, 1911-1919. 2019

[40] Sánchez-Molina, M., Amores, E., Rojas, N., & Kunowsky, M. Additive manufacturing of bipolar plates for hydrogen production in proton exchange membrane water electrolysis cells. International Journal of Hydrogen Energy, *(79)*, (46) 38983-38991. 2021

[41] Özdemir, S. N., & Taymaz, I. Three-dimensional modeling of gas–liquid flow in the anode bipolar plate of a PEM electrolyzer. Journal of the Brazilian Society of Mechanical Sciences and Engineering, *(44)*, (8) 354. 2022

[42] Lin, R., Lu, Y., Xu, J., Huo, J., & Cai, X. Investigation on performance of proton exchange membrane electrolyzer with different flow field structures. Applied Energy, *(326)*, 120011. 2022

[43] Roshandel, R., Arbabi, F., & Moghaddam, G. K. Simulation of an innovative flow-field design based on a bio inspired pattern for PEM fuel cells. Renewable Energy, *(41)*, 86-95. 2012

[44] Ruan, H., Wu, C., Liu, S., & Chen, T. Design and simulation of novel flow field plate geometry for proton exchange membrane fuel cells. Heat and Mass Transfer, *(52)*, 2167-2176. 2016

[45]   Asadzade, M., & Shamloo, A. Design and simulation of a novel bipolar plate based on lung-shaped bio-inspired flow pattern for PEM fuel cell. International Journal of Energy Research, *(41)*, (12) 1730-1739. 2017

[46]   Dong-Hui, W., Lin-Zhi, Y., Zhong-Yu, P., Cong-Da, L., Gang, L., & Qiao-Hui, L. A novel intersectant flow field of metal bipolar plate for proton exchange membrane fuel cell. International Journal of Energy Research, *(14)*, (41) 2184-2193. 2017

[47]   Trogadas, P., Cho, J. I. S., Neville, T. P., Marquis, J., Wu, B., Brett, D. J. L., & Coppens, M. O. A lung-inspired approach to scalable and robust fuel cell design. Energy & Environmental Science, *(1)*, (11) 136-143. 2018

[48]   Ouellette, D., Ozden, A., Ercelik, M., Colpan, C. O., Ganjehsarabi, H., Li, X., & Hamdullahpur, F. Assessment of different bio-inspired flow fields for direct methanol fuel cells through 3D modeling and experimental studies. International Journal of Hydrogen Energy, *(2)*, (43) 1152-1170. 2018

[49]   Kang, H. C., Jum, K. M., & Sohn, Y. J. Performance of unit PEM fuel cells with a leaf-vein-simulating flow field-patterned bipolar plate. International Journal of Hydrogen Energy, *(43)*, (44) 24036-24042. 2019

[50]   Dong, J., Liu, S., & Liu, S. Numerical investigation of novel bio-inspired flow field design scheme for PEM fuel cell. Journal of Renewable and Sustainable Energy, *(4)*, (12). 2020

[51]   Xiong, D., & Nadal, M. Linking water relations and hydraulics with photosynthesis. The Plant Journal, *(4)*, (101) 800-815. 2020

[52]   Brodribb, T. J., Feild, T. S., & Sack, L. Viewing leaf structure and evolution from a hydraulic perspective. Functional Plant Biology, *(6)*, (37) 488-498. 2010

[53]   Li, L., Nakajima, H., Moriyama, A., & Ito, K. Theoretical analysis of the effect of boiling on the electrolysis voltage of a polymer electrolyte membrane water electrolyzer (PEMWE). Journal of Power Sources, *(575)*, 233143. 2023

[54]   Upadhyay, M., Kim, A., Paramanantham, S. S., Kim, H., Lim, D., Lee, S., & Lim, H. Three-dimensional CFD simulation of proton exchange membrane water electrolyser: Performance assessment under different condition. Applied Energy, *(306)*, 118016. 2022

[55]   Lopata, J., Kang, Z., Young, J., Bender, G., Weidner, J. W., Cho, H. S., & Shimpalee, S. Resolving anodic current and temperature distributions in a polymer electrolyte membrane water electrolysis cell using a pseudo-two-phase computational fluid dynamics model. Journal of The Electrochemical Society, *(5)*, (168) 054518. 2021

[56]   Sato, H., Matsushima, H., Ueda, M., & Ito, H. Effect of water stoichiometry on deuterium isotope separation by anion exchange membrane water electrolysis. International Journal of Hydrogen Energy, *(68)*, (46) 33689-33695. 2021

[57]   Luo, Z., Chang, Z., Zhang, Y., Liu, Z., & Li, J. Electro-osmotic drag coefficient and proton conductivity in Nafion® membrane for PEMFC. International Journal of Hydrogen Energy, *(7)*, (35) 3120-3124. 2010

[58]   Dedigama, I., Ayers, K., Shearing, P. R., & Brett, D. J. An experimentally validated steady state polymer electrolyte membrane water electrolyser model. International Journal of Electrochemical Science, *(5)*, (9) 2662-2681. 2014

[59]   Zhou, H., Meng, K., Chen, W., & Chen, B. Exploratory research on bubbles migration behavior and mass transfer capacity evaluation of proton exchange membrane water electrolyzer based on a volume of fluid-coupled

electrochemical model. Energy Conversion and Management, *(290)*, 117217. 2023

CURRICULUM VITAE

PERSONAL INFORMATION

Name Surname   : Mohammad Naser ALOBEID
Date of Birth   :
Phone   :
E-mail   :

EDUCATION

High School   : East Riffa Secondary Boys School
Bachelor   : University of Bahrain
Master's degree   : Ankara Yıldırım Beyazıt University

TOPICS OF INTEREST

- Fluid Dynamics in Electrolysis
- Hydrogen Production and PEM Electrolysis
- Optimization Techniques
- Integration with Renewable Energy Sources
- Technological Advances in Water Electrolysis

PRESENT ORGANIZED PRESENTATION

- EJONS 16th INTERNATIONAL CONFERENCE ON MATHEMATICS, ENGINEERING, NATURAL & MEDICAL SCIENCES

  held on November 11-13, 2023 / Istanbul, Türkiye

- MASTER THESIS DEFENSE EXAMINATION

  held in 9, January, 2024 / Ankara, Türkiye